Petrography and geochemistry of fault-controlled hydrothermal dolomites in the Riópar area (Prebetic Zone, SE Spain)

Dídac Navarro-Ciurana[1*], Mercè Corbella[1], Esteve Cardellach[1], Elena Vindel[2], David Gómez-Gras[1], Albert Griera[1]

[1]Departament de Geologia, Facultat de Ciències, Universitat Autònoma de Barcelona, Edifici Cs s/n, 08193 Bellaterra (Cerdanyola del Vallès), Spain

[2]Departamento de Cristalografía y Mineralogía, Facultat de Ciencias Geológicas, Universitat Complutense de Madrid, c/ José Antonio Novais s/n, 28040, Madrid, Spain

*Corresponding author (e-mail: didac.navarro.ciurana@gmail.com)

ABSTRACT: The present paper reports the first detailed petrographical and geochemical studies of hydrothermal dolomites related to MVT Zn-(Fe-Pb) deposits in the Riópar area (Mesozoic Prebetic Basin, SE Spain), constraining the nature, origin and evolution of dolomitizing and ore-forming fluids. Mapping and stratigraphic studies revealed two stratabound dolostone geobodies connected by other patchy bodies, which replace carbonate units of Upper Jurassic to Lower Cretaceous ages. These dolostones are associated to the W-E trending San Jorge fault, indicating a main tectonic control for fluid flow. Seven different dolomite types were identified: i) matrix-replacive planar-s (ReD-I); ii) matrix-replacive planar-e (ReD-II); iii) planar-e sucrosic cement (SuD); iv) non-planar grey saddle dolomite cement (SaD-I) pre-dating Zn-(Fe-Pb) sulfides; v) non-planar milky to pinkish saddle dolomite cement (SaD-II) post-dating Zn-(Fe-Pb) ores; vi) ore-replacive planar-e porphyrotopic (PoD); and vii) planar-s cloudy cement (CeD). Meteoric calcite types were also recognized. The different dolomite types are

isotopically characterized by: i) depleted $\delta^{18}O$ (from +25.1 to +27.6‰ V-SMOW) and $\delta^{13}C$ (from -2.3 to +0.9‰ V-PDB) values compared to Upper Jurassic to Lower Cretaceous limestone signature ($\delta^{18}O$: +27.6 to +30.9‰ V-SMOW; $\delta^{13}C$: +0.5 to +3.2‰ V-PDB); and ii) $^{87}Sr/^{86}Sr$ ratios for the main dolomitization phases (ReD and SuD: 0.70736-0.70773) close to the Jurassic and Cretaceous carbonate values (0.70723-0.70731) whereas more radiogenic values (0.70741-0.70830) for saddle dolomites (SaD) related to the Zn-(Fe-Pb) sulfide mineralization prevailed after fluid interaction with Rb-bearing minerals. Microthermometrical studies on two-phase liquid and vapor fluid inclusion populations in planar and non-planar dolomites and sphalerite show homogenization temperatures between 150 and 250ºC. These data indicate that both planar and non-planar dolomite textures formed at high-temperatures under hydrothermal conditions in deep-burial diagenetic environments. The main dolomitizing phase (ReD-I/ReD-II and SaD-I) shows low to moderate fluid inclusions salinity (5 to 14 wt.% eq. NaCl), whereas the dolomitization related to ore precipitation (sphalerite and SaD-II) spreads to higher salinity values (5 to 25 wt.% eq. NaCl). These data may respond to a mixing between a low salinity fluid (fluid A, less than 5 wt.% eq. NaCl) and a more saline brine (fluid B, more than 25 wt.% eq. NaCl) at different fluid proportions.

KEYWORDS: Dolomitization; Hydrothermal fluids; Isotope geochemistry; Fluid inclusions; Riópar; Prebetic Zone; Southeast Spain

1   Introduction

The study of dolostones and dolomitizing processes is of a great interest as the resulting rocks may host economic base-metals Zn-Pb-F ore-deposits (i.e. Mississippi Valley-Type (MVT) and Sedimentary Exhalative (SEDEX); Leach and Sangster, 1993; Muchez et al., 2005) and more than half of the world's hydrocarbon reserves (e.g. Zenger et al., 1980; Warren, 2000; Davies and Smith, 2006). Actually, more than 80% of recoverable oil and gas of North American reservoirs occur in dolomitized carbonates (e.g. Braithwaite et al., 2004). Due to intense hydrocarbon subsurface exploration, examples of oil and gas reservoirs in Paleozoic dolomitic rocks are well known (e.g. Davies and Smith, 2006; Hannigan et al., 2006; Morrow, 2014), but fewer cases hosted in Mesozoic dolomites have been studied (e.g. Ameen et al., 2010; Swart et al., 2015). The key factors controlling the occurrence and distribution of viable Mesozoic dolostone reservoirs remain insufficiently understood and their outcrop analogues are poorly studied.

Most of the known burial dolostone occurrences have an important tectonic control: extensional and/or transtensional faults are particularly common geodynamical settings (e.g. Duggan et al., 2001; Sharp et al., 2010). Structurally-controlled dolostones commonly involve hot fluids, defining the so called hydrothermal dolomites (HTD) (e.g. Davies and Smith, 2006; Smith and Davies, 2006), formed when the temperature of the dolomitizing fluid is 5ºC or higher than that of the host rock (White, 1957). The HTD geobodies can result in a variety of geometries, but the most common are: i) stratabound and tabular-shaped dolostone bodies which extend away from fault zones following suitable layers (e.g. Sharp et al., 2010; Lapponi et al., 2011; Martín-Martín et al., 2013; Dewit et al., 2014); ii) fault-related irregular dolostones distributed in patches along fault traces (e.g. Duggan et al., 2001; Wilson et al., 2007; López-Horgue et al., 2010); and iii) Christmas-tree like morphology, that results from stratabound end

members and a patchy combination in individual dolostone bodies (e.g. Sharp et al., 2010).

In the Riópar area (Prebetic, SE Spain) dolomitization bodies spatially related to Zn-(Fe-Pb) mineralizations are hosted in Upper Jurassic to Lower Cretaceous carbonatic sequences. A first attempt to understand the relationship between dolomitization and mineralization in the area was done by Grandia et al. (2001), which was focused on petrographical studies. In the present paper we provide new petrographical and geochemical data in order to better understand the origin and evolution of dolomitizing fluids and the relationship with Zn-(Fe-Pb) occurrences in the area. Microthermometrical studies to constrain the composition, temperature and origin of dolomitizing fluids are also presented.

2   Geological setting

The study area is located near the Riópar village (Albacete province, SE Spain; Fig. 1), where Mesozoic siliciclastics, limestones and dolostones occur. This area is situated at the limit between the Internal and External Prebetic Zones (Fig. 1), a broad Alpine tectonic unit that corresponds to the outer portion of the fold-and-thrust belt of the Betic Cordillera (e.g. García-Hernández et al., 1980). It comprises Mesozoic to Cenozoic carbonates and clastics sequences up to 2000 m thick, originally deposited in the southern part of the Iberian continental paleomargin (Vera et al., 2004). The foreland NNW-verging Prebetic fold-and-thrust belt became detached from the Variscan basement along Upper Triassic sediments (Fig. 2) during the Miocene main orogenic stage (e.g. Barbero and López-Garrido, 2006). The External Prebetic Zone, dominated by shallow internal platform facies, corresponds to the deformed part of the

4

septentrional basin where frequent stratigraphic gaps are observed. This zone is characterized by extensively exposed Triassic and Jurassic rocks, scarce Cretaceous materials and absence of Paleogene sediments. This is in contrast with the Internal Prebetic Zone, which is dominated by marginal platform to slope facies and large fold and thrust structures with absence of Triassic rocks, scarcity of Jurassic strata and extensive outcrops of Cretaceous and Paleogene sediments (Fig. 2) (e.g. García-Hernández et al., 1980; Vera et al., 2004).
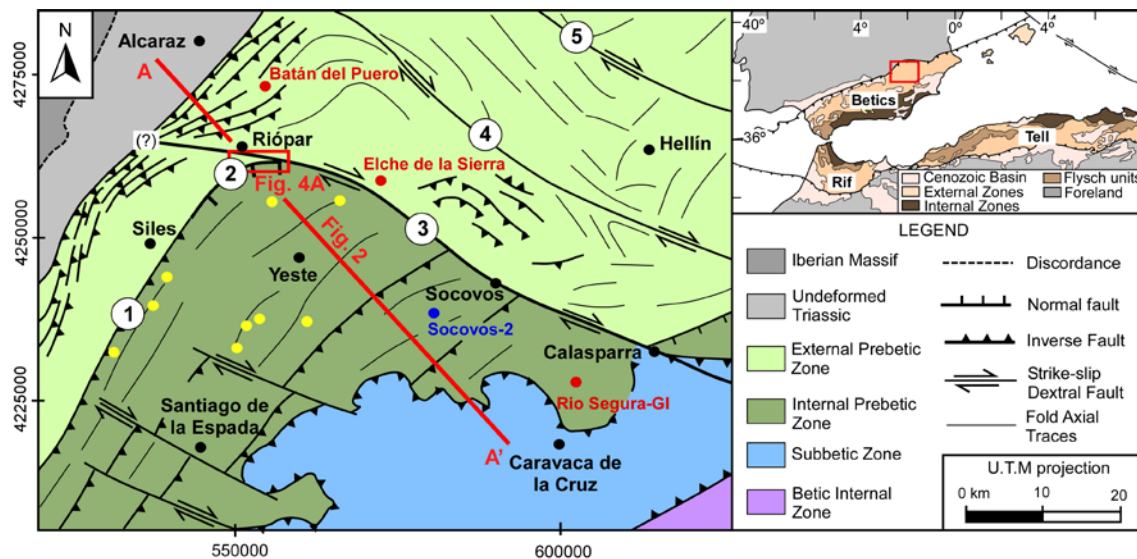

Figure 1. Geological and tectonic sketch of Prebetic Zone (Betic Cordillera), modified from Pérez-Valera et al. (2010) (see Figure 2 for geologic cross-section in direction A-A' and Figure 4a for detailed geological map of the studied area). The inset in the upper right corner shows the location of the studied area in the Betic Range (Comas et al., 1999). Numbers in circles refer to: (1) Alto Guadalquivir fault; (2) San Jorge Fault; (3) Socovos-Calasparra fault; (4) Liétor fault; and (5) Pozohondo fault. Color dots refer to location of: subsidence analyses performed by Hanne et al. (2003) (red); vitrinite reflectance analyses from Albian sandstones samples conducted by Barbero et al. (2001)

(blue); and apatite fission-track thermal model analyses from Cretaceous samples performed by Barbero and López-Garrido (2006) (yellow).

2.1 Tectonic evolution

The evolution of the Mesozoic tectonic basin in the Prebetic margin started in Late Permian-Early Triassic age with an intracontinental rifting (Fig. 3) related to the Tethys Ocean opening and to the dismembering of the Pangea supercontinent by the divergence of the European and African plates (Banks and Warburton, 1991; Barbero and López-Garrido, 2006). This initial phase was followed by a post-rifting stage during Early to Middle Jurassic ages (Fig. 3) with development of shallow carbonate platforms (e.g. García-Hernández et al., 1980). A second main extensional stage occurred during Late Jurassic to Early Cretaceous ages (Fig. 3), which was related to the opening of the North Atlantic Ocean by the separation of Iberian and African plates (e.g. Banks and Warburton, 1991; Arias et al., 1996). This later rifting period allowed the development of subsident troughs and pelagic highs, differentiating the Internal and External Prebetic Zones from the rest of the Betic basin (e.g. Vilas et al., 2001). A post-extensional thermal subsidence period occurred during Albian to Late Cretaceous ages (Fig. 3), when the African plate approached the Iberian plate (Barbero and López-Garrido, 2006), developing extensive shallow-marine carbonate platforms in the Iberian margins.
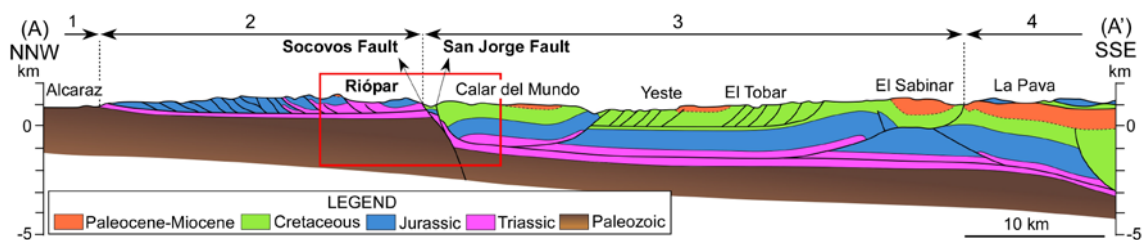

Figure 2. Geologic cross-section of the Prebetic Zone (see Figure 1 for location) according to Banks and Warburton (1991). The cross-section part into the red square is

modified according our field geologic data. Numbers refer to: (1) Iberian Massif; (2) External Prebetic Zone; (3) Internal Prebetic Zone; and (4) Subbetic Zone.

Paleogene basins in the Prebetic Zones started to develop under compressive conditions related to the early stages of the Alpine Orogeny (Vera et al., 2004). All of these deposits were overlain by Lower to Middle Miocene transgressive marine sin-orogenic sediments, which pass upwards into Upper Miocene continental post-orogenic deposits (e.g. Calvo et al., 1978; Montenat et al., 1996). The destruction of the Prebetic margin due to the convergence of the African and Iberian plates started in Paleogene times, but the main collision event occurred in the Miocene (Fig. 3) with the structuring of the Betic Chain (Barbero and López-Garrido, 2006).

From a tectonic standpoint, the Prebetic Zones are characterized by the Cazorla-Alcaraz-Hellín structural arc which developed in the transition from Middle to Upper Miocene (Rodríguez-Pascua et al., 2000; Fig. 1). In general, it is constituted by two major system faults: i) NE-SW trending and SE dipping faults; and ii) NW-SE trending subvertical dextral strike-slip faults perpendicular to the fold axes (Fig. 1).

2.2   Lithostratigraphy

A large number of Mesozoic sedimentary units, grouped in four stratigraphic megasequence, have been proposed (Fig. 3), based on field observations and previously published works (e.g. Rodríguez-Estrella, 1979; Martín-Chivelet, 1994; Vera et al., 2004, among others). The studied dolomites at Riópar are hosted in the third of these megasequences, which corresponds to Upper Jurassic to Lower Cretaceous (Middle Kimmeridgian to Aptian) carbonate formations. The Upper Jurassic stratigraphic succession is formed by the Lower and Middle Members of Sierra del Pozo Fm (Middle

Kimmeridgian to Lower Berriasian). It shows highly dolomitized oosparitic grainstones to packstones (Fig. 3a) and rhythmic gray nodular limestones and marls (Fig. 3b) partly dolomitized with fine siliciclastic interbedded layers. The partially dolomitized Lower Cretaceous succession corresponds to the Upper Mb of Sierra del Pozo Fm, Cerro Lobo Fm and Arroyo de los Anchos Fm (Upper Berriasian to Aptian). The Upper Mb of Sierra del Pozo Fm is constituted by grey dolomitized intra-oosparitic grainstones to packstones (Fig. 3b). The Cerro Lobo Fm shows a brownish marl and limestone rhythmic sequence with millimetric to centimetric lignite levels (Fig. 3c). Two partially dolomitized units have been differentiated in the Arroyo de los Anchos Fm: the Lower Mb is formed by grey intraclastic black pebbles ("cailloux noire") limestones (Fig. 3d) and the Upper Mb corresponds to brownish ferruginous pisolitic limestones. This megasequence was formed in an extension tectonic setting (Fig. 3) with development of deep-epicontinental to tidal carbonate platforms with terrigenous components (e.g. García-Hernández et al., 1980; Vera et al., 2004).

3   Methods and sampling

New detailed mapping of the Riópar area was carried out in order to understand the geometry of the dolomite bodies, the dolomite facies and textural zonings along the dolomite bodies at a large scale. Systematic sampling was performed across the different dolomite bodies as well as from underground workings, dumps and surface outcrops from the Zn-(Fe-Pb) mineralized areas. A total of 145 polished thin sections of dolomites were studied in detail using petrographic microscopy. Selected thin sections were previously half stained with alizarin red-S and K-ferricyanide (Dickson, 1966) to differentiate ferroan/non-ferroan dolomite and calcite. Cathodoluminescence (CL)

8

analyses were carried out in representative thin sections using a Technosyn 8200 MarkII cold-cathode electron-gun mounted on a polarizing microscope at the *Dpt. de Geoquímica, Petrologia i Prospecció Geològica* of the *Universitat de Barcelona (UB)*.
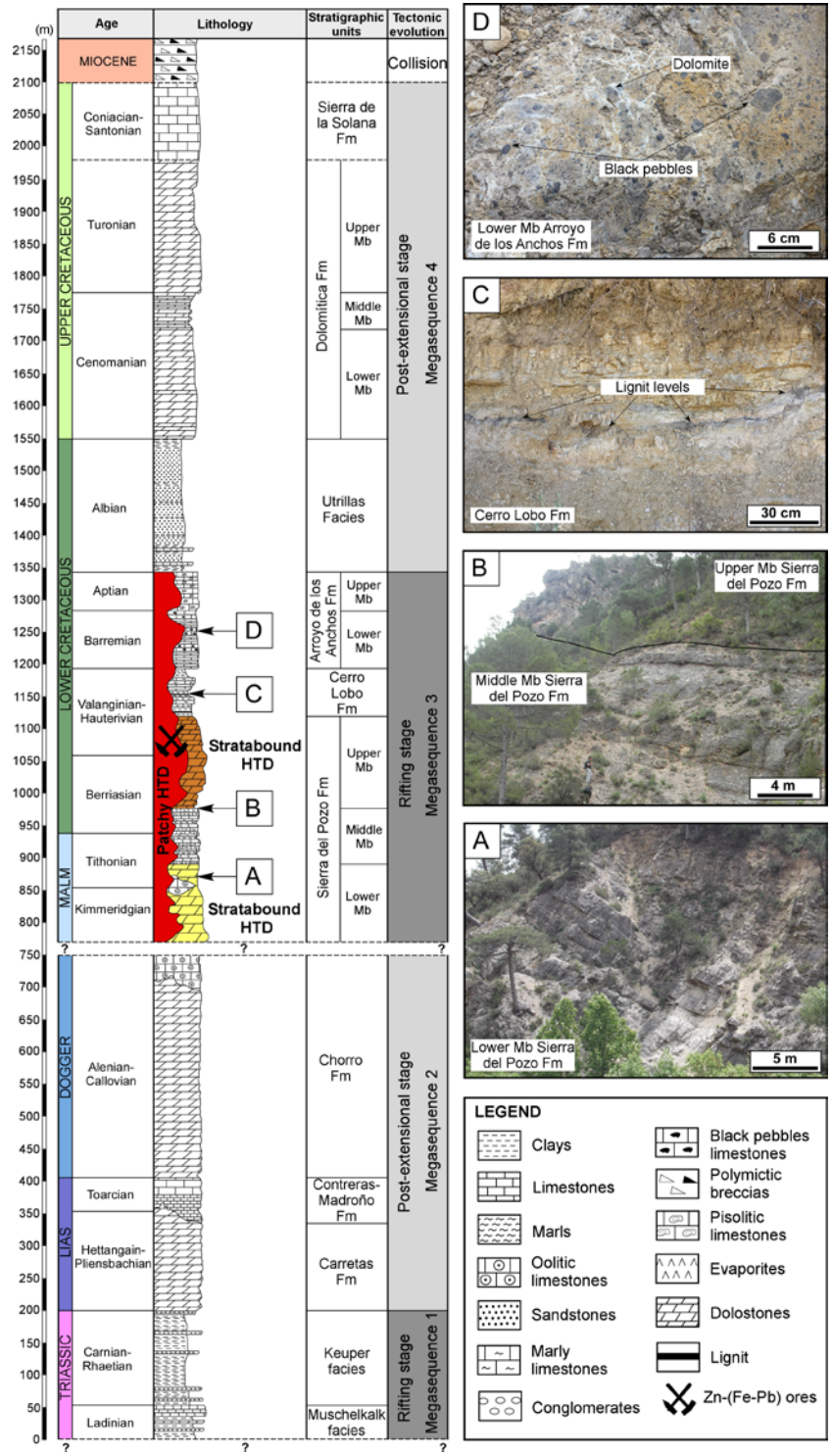
Figure 3. Stratigraphic section of the Riópar area with sedimentary units and sequences, location of the studied dolomite bodies and Zn-(Fe-Pb) ores and tectonic evolution of the Prebetic Zone according to Barbero and López-Garrido (2006). (A) Microcrystalline dolostone from the Lower Mb of Sierra del Pozo Fm. (B) Contact between Middle (limestone and marls) and Upper (dolostones) Members of Sierra del Pozo Fm. (C) Limestone and marls with lignite levels of Cerro Lobo Fm. (D) Limestone with black pebbles ("cailloux noire") from the Lower Mb of Arroyo de los Anchos Fm.

Mg, Ca, Fe, Zn and Na analysis of different dolomite type crystals from representative polished thin sections were performed by Electron Microprobe (EMP) using a JEOL JXA 8900, equipped with four wavelength dispersive spectrometers and an energy dispersive spectrometer, at the *ICTS Centro Nacional de Microscopía Electrónica* of the *Universidad Complutense de Madrid (UCM)*. The operation conditions were 15 kV accelerating voltage, 10 nA beam current, 5 µm beam diameter and counting time of 20 s per element. The calibration standards used were: dolomite (Ca, PET, Kα and Mg, TAP, Kα), siderite (Fe, LIF, Kα), sphalerite (Zn, LIFH, Kα) and strontianite (Sr, PETH, Lα). Whole-rock trace strontium composition of different dolomite types were determined in ActLabs, Canada, by a lithium metaborate/tetraborate fusion Inductively Coupled Plasma-Mass Spectometer (ICP-MS).

Different dolomite and calcite types and host limestones were sampled using a microdrilling device for carbon, oxygen and strontium isotope analysis, performed at the *Centres Científics i Tecnològics* of the *UB* (CCiTUB) and the *Centros de Apoyo a la Invetigación* (*CAI)* of the *UCM* respectively. For C and O isotope compositions up to 30 mg of sample was reacted with anhydrous phosphoric acid (H_3PO_4) at 50ºC, and the

collected CO_2 was analyzed in a Finnigan MAT Delta S thermal ionization mass spectrometer. The standard deviation was better than $\pm0.1‰$ (1σ) for both $\delta^{13}C$ and $\delta^{18}O$. Results are presented as permil deviation with respect to V-PDB for carbon and to V-SMOW and V-PDB for oxygen (see Table 1). For Sr isotope analyses, 50 to 100 mg of sample powders was dissolved in 2.5N HCl at 80ºC, dried, and redissolved using 3M HNO_3. The strontium aliquots were extracted using the conventional cation exchange procedures, and the $^{87}Sr/^{86}Sr$ ratios were analyzed in a TIMS-Phonix thermal ionization mass spectrometer. The reproducibility (2σ) was better than $\pm0.03\%$.

Doubly polished sections were prepared for the petrographic and microthermometric studies of fluid inclusions. The presence and distribution of hydrocarbon fluid inclusions were studied using a photoluminescence microscopy (Nikon Optiphot, equipped with a blue-violet excitation fluorescence filter) at the *Dpt. de Geoquímica, Petrologia i Prospecció Geològica* of the *UB*. Microthermometric measurements were carried out using a Linkam THMS-600 heating-freezing stage at the *Dpt. de Geologia* of the *Universitat Autònoma de Barcelona* (UAB). Temperatures were calibrated from the melting of synthetic H_2O-CO_2 fluid inclusions (-56.6ºC), melting of ice and critical homogenization at 220 bar (374.1ºC) of synthetic H_2O inclusions in quartz. The precision of the measurements was ±0.2ºC below 0ºC and ±2ºC for the homogenization temperatures. Homogenization measurements were carried out before freezing runs to avoid stretching of fluid inclusions by ice nucleation. Salinities of fluid inclusions were estimated using the program *AqSo2* from the computer package *FLUIDS* (Bakker, 2003).

4   Field observations

The studied dolostones outcrop over an area of 4.6 km^2 between the footwall block of the extensive W-E trending, S-dipping San Jorge fault and the Socovos dextral strike-slip fault. Diapirs of Triassic clays and evaporites (Keuper facies) were identified in the area, probably causing the flexure of adjacent and overlying strata (Fig. 4). Two types of dolostone geobodies have been distinguished: one characterized by grey to brown color and stratabound morphology, which develops into a second type of white patchy dolostone (Fig. 5a). The resulting dolomite geobodies may be conceived as a Christmas-tree like morphology (Fig. 4), although it is not well observed in the field.

Two stratabound dolostones are identified, affecting the Lower and the Upper Mb of Sierra del Pozo carbonates respectively (Figs. 3 and 4), preserving the original depositional fabrics (e.g. stratification, lamination). The Lower Mb of Sierra del Pozo Fm is partially dolomitized as it conserves oolitic limestone lenses (Fig. 4); the dolostones contain abundant oolitic moldic porosity and ghosts (Fig. 6a). However, the Upper Mb has always been observed as a completely dolomitized unit, with abundant orbitolinid moldic porosity (Fig. 5b). The stratabound dolomitization fronts are locally wavy but commonly follow the main bedding (Figs. 3b and 4). These dolostones are constituted by fine microcrystalline dolomite (FmD: Fig. 5a).

Patchy dolostones outcrop in separate bodies observed from the Lower Member of Sierra del Pozo to the Arroyo de los Anchos Fms (Figs. 3 and 4). These dolostones partially obliterate the original sedimentary fabric (Fig. 5a). As they are hosted in the same Upper Jurassic to Lower Cretaceous carbonates, the different patches can be considered as a single dolostone body. The patchy dolomitization front is sharp with the undolomitized carbonates, cross-cutting bedding and stratification. Nevertheless, the contact with the stratabound dolostone units is irregular and gradational, with a gradual color change from white to grey (Fig. 5a). Patchy dolostones

are constituted by sucrosic (SuD) and saddle dolomite (SaD) phases. Besides the larger bodies, saddle dolomite is also found forming rhythmic textures, cementing breccias around small fractures and along stratification surfaces within the stratabound dolostones (Figs. 5c and 5d).
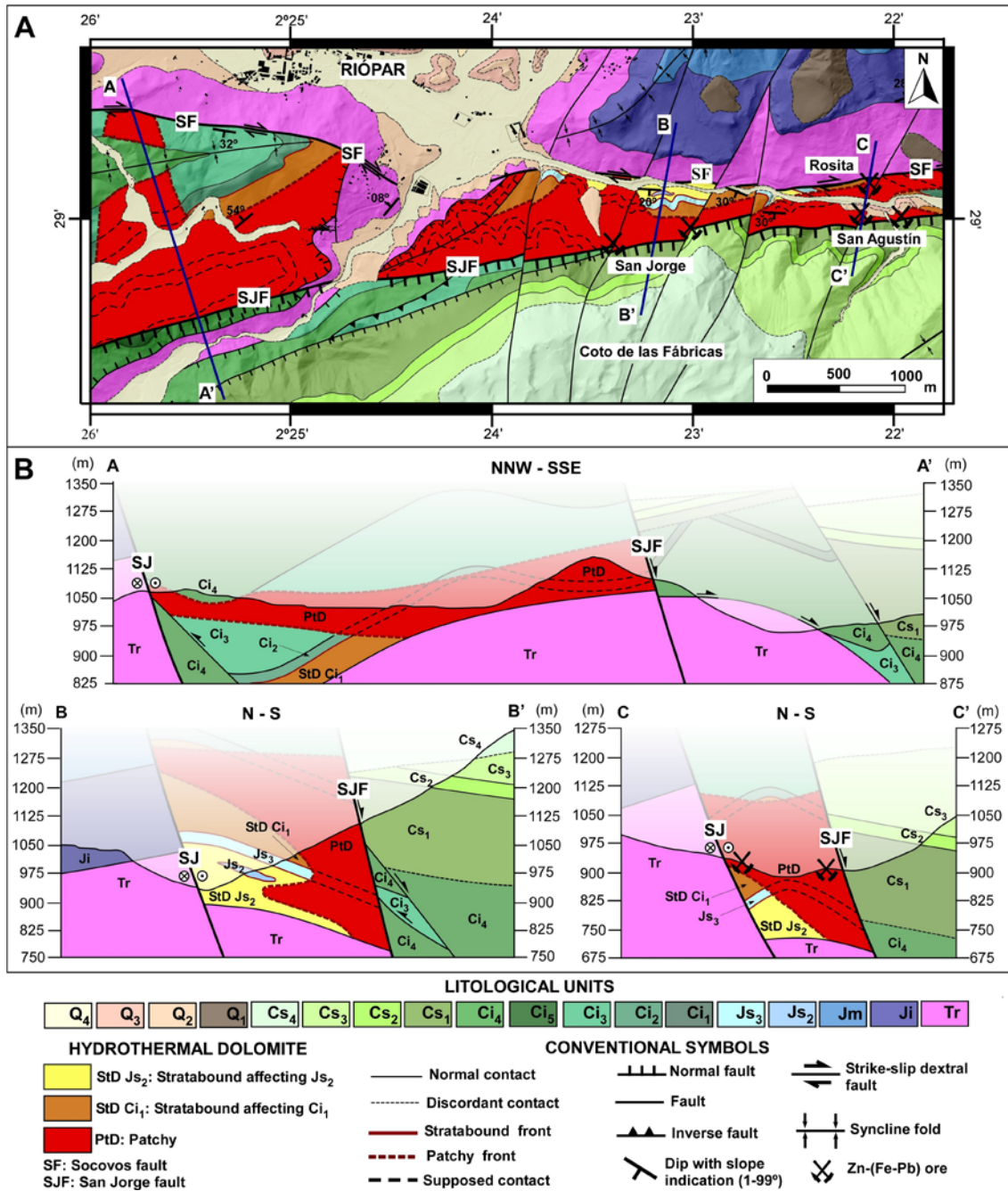

Figure 4. Detailed geological map (A) and geologic cross sections (B) of the Riópar area with distribution and morphology of the studied dolostone bodies. Tr: Triassic

13

clays and sandstones; Ji: Lower Jurassic dolostones; Jm: Middle Jurassic dolostones; Js$_2$, Js$_3$, Ci$_1$: Sierra del Pozo Fm; Ci$_2$: Cerro Lobo Fm; Ci$_3$: Arroyo de los Anchos Fm; Ci$_4$: sandstones and clays of Utrillas facies; Ci$_5$: dolostones of Utrillas facies; Cs$_1$, Cs$_2$, Cs$_3$: Cenomanian-Turonian dolostones; Cs$_4$: Coniacian-Santonian limestones; Q$_1$: undifferentiated colluvium; Q$_2$: alluvial fans; Q$_3$: debris on alluvial funs; Q$_4$: debris on hillsides.
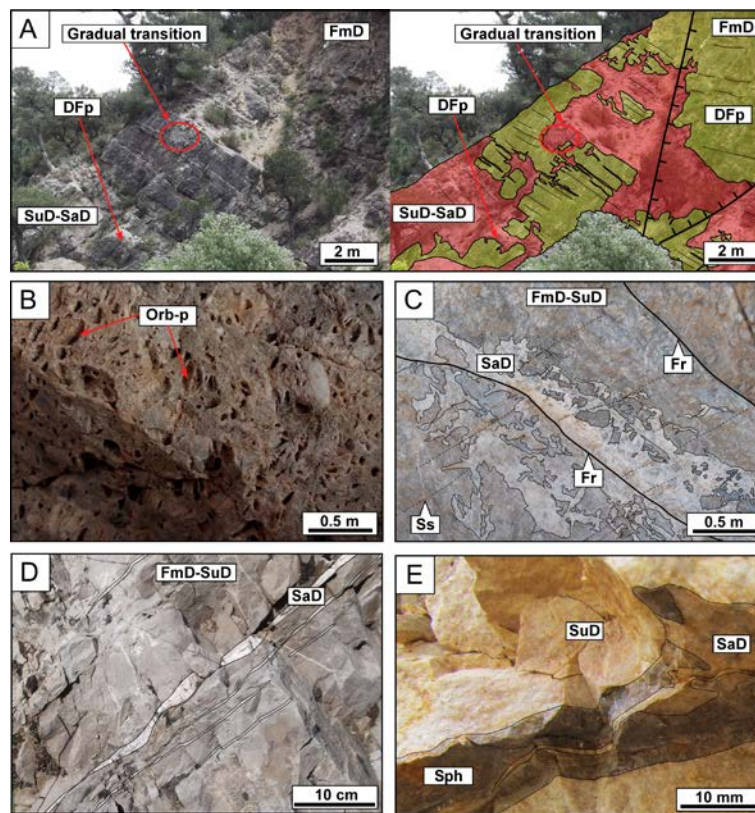

Figure 5. Outcrop photographs of dolostones occurrences associated with Zn-(Fe-Pb) ores in the Riópar area (SE Spain). (A) Fine microcrystalline stratabound dolostone (FmD: grey to brown color) of the Lower Mb of Sierra del Pozo Fm, preserving the original stratification and associated with patchy sucrosic and saddle dolostones (SuD-SaD: whitish to greyish color) which are fabric destructive. Note the irregular dolomitization front of patchy dolostone (DFp), which cross cut the main stratification planes (Ss), showing gradual color change from white to grey. (B) Orbitolinid moldic

14

porosity (Orb-p) from the Upper Mb of Sierra del Pozo stratabound dolostone. (C) Saddle dolomite cementing breccias along secondary fractures (Fr) and crosscutting stratification planes (Ss). (D) Saddle dolomite along stratigraphic planes. (E) Dolomite vein associated with massive sphalerite (Sph).

Zn-(Fe-Pb) sulfide ores (Fig. 5e) are hosted in dolomitized limestones of the Upper Mb of Sierra del Pozo Fm (Figs. 3 and 4). The Riópar deposits were mined since 1773 and produced a minimum of ~20,000 t of Zn along its mining history. They occur as disseminations in microcrystalline stratabound dolostones and millimetric to centimetric size veinlets associated with saddle dolomite hosted in patchy dolostones (Fig. 5e). As the Upper Jurassic and Lower Cretaceous succession does not outcrop in the hanging block of the San Jorge fault, the presence of the same dolomitizing and mineralizing process in it cannot be confirmed.

5 Petrography

5.1 Dolomite types

Different types of dolomite have been recognized. Their descriptions follow the dolomite classification of Gregg and Sibley (1984) and Sibley and Gregg (1987).

5.1.1 Matrix-replacive planar-s (ReD-I) and planar-e (ReD-II) dolomites

Replacive dolomite (ReD-I) is characterized by its brownish to grayish color on weathered surfaces. Under microscopic viewing, ReD-I shows minor to dense packing of equigranular crystals with sizes ranging from 10 to 30 μm (Figs. 6a and 6b). Dolomite shapes are mostly subhedral and in minor grade anhedral with cloudy

appearance (inclusion-rich), with oval and serrated crystal boundaries. ReD-II shows inequigranular crystals with sizes of less than 1 mm (Fig. 6c). Dolomite crystal shapes are euhedral with alternating cloudy (inclusion-rich) and clear (inclusion-poor) bands. In addition, transitions of planar subhedral to euhedral dolomites (ReD-I/ReD-II) are frequent, showing crystal sizes from 10 to 50 μm. Most of the ReD-I and ReD-II crystals are cloudy under plane polarized light with dominant straight extinction under cross polarized light. These dolomites are slightly ferroan as indicated by its pale blue color staining and have a characteristic homogenous bright red luminescence (Fig. 6b).

ReD pervasively replaces the Lower and Upper Member of Sierra del Pozo Fm limestones, forming the stratabound dolostones. This is evidenced by the presence of original limestone relicts, moldic porosity and ghosts, predominantly micritized ooids (Figs. 6a and 6b) and orbitolinids (Fig. 5b) and to a lesser extent peloids and intraclasts. However ReD-II occurs as porphyrotopic floating- to contacting-rhombs replacing selectively micritic compounds, often observed at the contact between dolomite bodies and host limestones (Fig. 6c). Disseminated Zn-(Fe-Pb) sulfides are found related to this dolomite type.

5.1.2 Planar-e sucrosic dolomite cements (SuD)

SuD is characterized by its whitish color in fresh rock. Under microscope examination, it shows very minor to dense packing of inequigranular crystals with medium to coarse sizes (250 μm to 2 mm). Micrometer intercrystalline and millimeter to centimeter vuggy porosity is well developed (around 15%) (Figs. 6d and 6g). This dolomite type is euhedral with rhombohedral morphologies showing mainly cloudy (inclusion-rich) centers and clear (inclusion-poor) borders (Fig. 6d) and straight extinction under crossed polarized light. It is non-ferroan to slightly ferroan as indicated by the non to

pale blue staining with K-ferricyanide. Under CL, the clear borders show dull red and bright orange luminescence rims (Fig. 6e) with moderately corroded crystal borders. SuD is observed hosted in the Lower Member of Sierra del Pozo to Arroyo de los Anchos Fms.
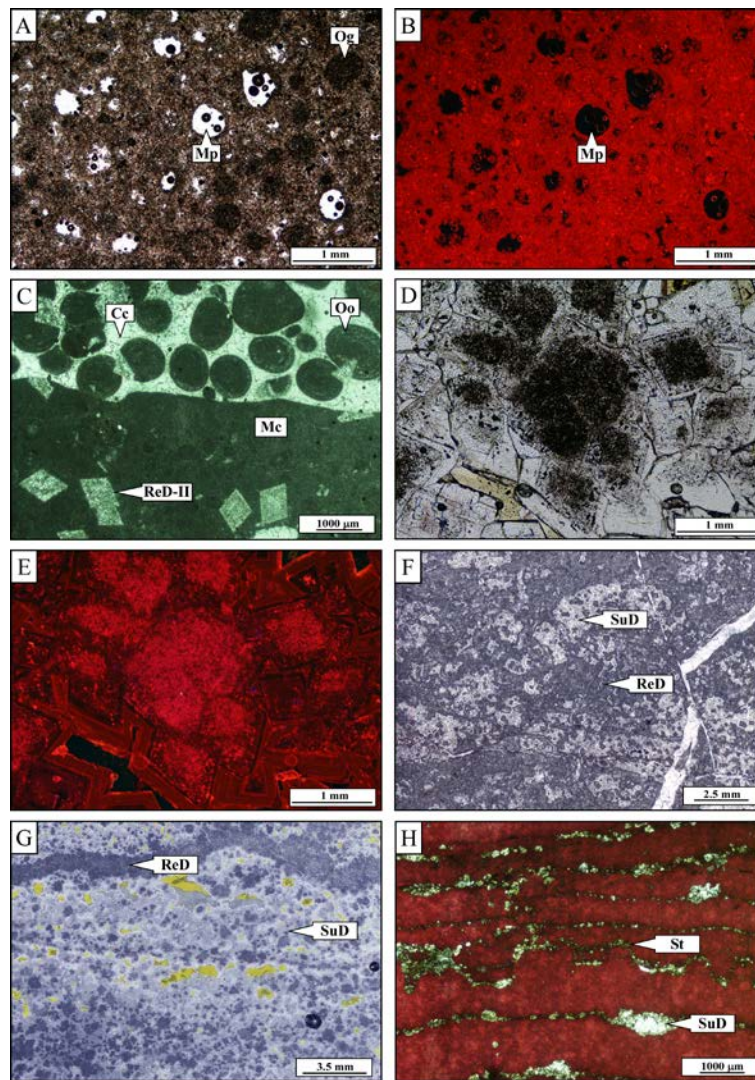

Figure 6. Petrographic characteristics of matrix-replacive planar-s (ReD-I) and planar-e (ReD-II) dolomites, as well as planar-e sucrosic dolomite cements (SuD). (A) Transmitted light (TL) microphotograph of equigranular ReD-I with mosaic fabric, oolitic ghosts (Og) and moldic porosity (Mp) derived from dissolution of ooids. (B) Cathodoluminescence (CL) microphotograph of ReD-I with bright red luminescence.

(C) ReD-II (dedolomitized) replacing selectively micritic (Mc) and micritized oolitic (Oo) compounds cemented by calcite (Cc) (TL). (D) TL photomicrograph of SuD showing cloudy centers and light borders and intercrystalline porosity (yellow color). (E) CL image of SuD with center relicts of ReD. (F) Pocket dolomite fabric consisting of ReD and SuD dolomites (TL). (G) Rhythmic dolomite fabric consisting of ReD and SuD alternating bands with good porosity development (yellow color) (TL). (H) SuD crystallization along stylolites (St) and affecting the nodular limestones of the Middle Mb of Sierra del Pozo Fm (red color is calcite stained by K-ferricyanide) (TL).

SuD often occurs as ReD recrystallization, observed by the presence of cloudy crystal centers that correspond to precursor dolomite ghosts with their characteristic bright red luminescence (Figs. 6d and 6e). SuD has also been identified as ReD overgrowths, whose crystals are characterized by irregular to planar boundaries, with its size increasing outwards. SuD may show pocket dolomite fabrics (Fig. 6f) or rhythmic textures (Fig. 6g) and has been observed cementing and filling host limestone stylolites (Fig. 6h).

5.1.3   Non-planar saddle dolomite cements (SaD)

SaD shows slightly curved faces, cleavage traces and sweeping extinction under cross polarized light. Two saddle dolomite types were identified: grey (SaD-I) and milky to pinkish (SaD-II). SaD-I is composed of densely packed equigranular crystals of fine to medium size (50 μm to 5 mm) and cloudy appearance (inclusion-rich: Fig. 7a). Under CL, SaD-I shows growth zoning with bright to dull-dark red alternations (Fig. 7b). SaD-II forms densely packed inequigranular crystals with coarse- to very coarse-size (500 μm to 1 cm). It always occurs as zoned crystals showing cloudy (inclusion-rich) and

clear (inclusion-poor) alternating rims (Fig. 7c). The cloudy and clear rims show strong growth zoning with bright orange to red, dull-dark red and non-luminescence alternating bands (Fig. 7d). Both types appear to be non-ferroan to slightly ferroan as indicated by the non-staining to pale blue staining color with K-ferricyanide.

SaD occurs as: i) ReD and SuD recrystallization, with gradual transitions (Figs. 7a and 7b); ii) ReD and SuD overgrowths, with irregular transitional contacts and gradual grain size increases (Fig. 7e) with developments of rhythmic textures (Figs. 7f and 7g); iii) millimetric to centimetric veins that crosscut the previous dolomites (Fig. 7h) usually containing Zn-(Fe-Pb) sulfides; and iv) cementing dolostone clasts (ReD-I/ReD-II) in fracture-controlled breccias (Fig. 5c). SaD-I pre-dates Zn-(Fe-Pb) sulfides, whereas SaD-II fills remnant porosity after SaD-I and sulfide precipitation (Fig. 8).

5.1.4   Ore-replacive planar-e porphyrotopic dolomite (PoD)

PoD forms euhedral crystals with porphyrotopic rhombohedral morphologies showing cloudy nucleus centers and clear rims, in some cases with unusual pleochroism. It shows inequigranular crystals with medium to coarse grain sizes (30 to 500µm: Fig. 8a) and straight extinction under crossed polarized light. It is ferroan in composition, showing bright clear red centers and dull dark red luminescence borders (Fig. 8b), although no minor elements zonation was distinguished in backscattered electron microprobe images (Fig. 8c). PoD has been observed extensively replacing Zn sulfide mineralization (Figs. 8a and 8c).

5.1.5   Planar-s cloudy dolomite cement (CeD)

CeD consists of densely packed anhedral crystals with very fine sizes (less than 20µm). It occurs as white veinlets that crosscut all previous dolomite phases (Fig. 8d) and, in a

lesser extent, Zn-(Fe-Pb) sulfides. Also, CeD is non-ferroan to slightly ferroan and CL observations revealed dull patchy red luminescence crystals (Fig. 8e). Moreover, no elemental composition differences were observed in backscattered electron microprobe images (Fig. 8c).
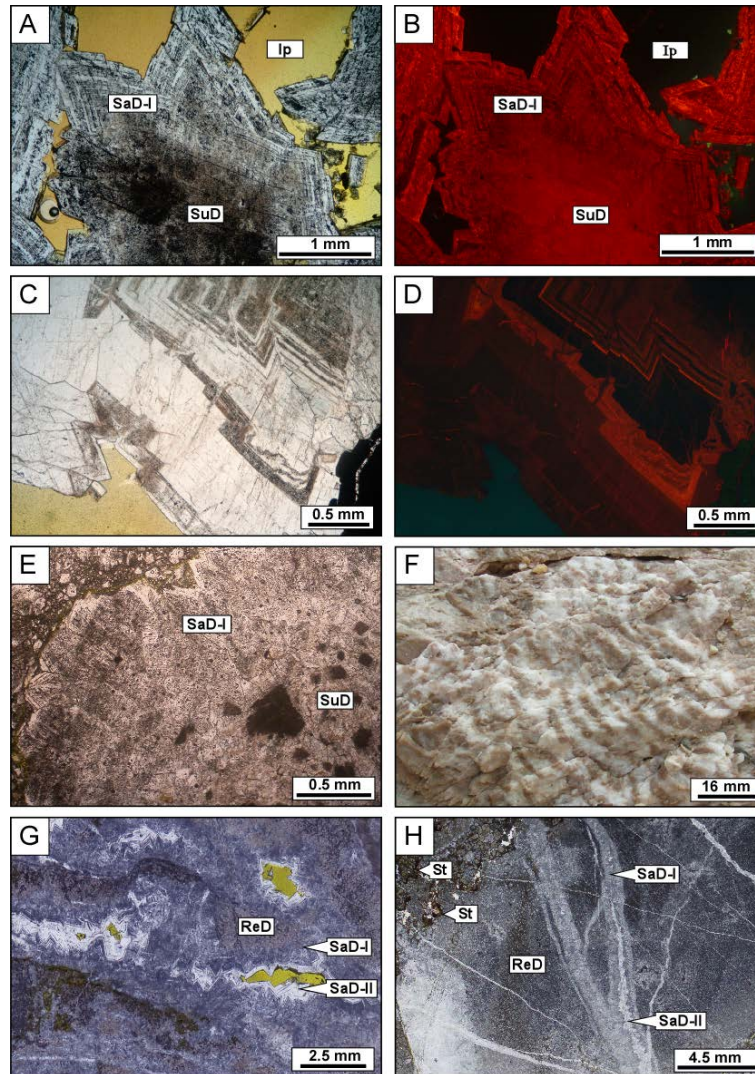

Figure 7. Petrographic observations of saddle dolomite types. (A) Transmitted light (TL) microphotograph of SaD-I showing cloudy centers that consists of SuD with well-developed intercrystalline porosity (Ip: yellow zones). (B) Cathodoluminescence (CL) microphotograph of SaD-I. (C) Detailed TL microphotograph of SaD-II showing alternating clear and cloudy alternating bands. (D) CL microphotograph of SaD-II

showing alternating luminescence and non-luminescence bands. (E) Transition of SuD to SaD-I by aggrading crystal size. (F) Hand specimen showing interlayered brown and white dolomite exhibiting rhythmic dolomite texture. (G) Transition from ReD to SaD-I and SaD-II bands from rhythmic dolomite sample with intercrystalline porosity (yellow color). (H) Fractures filling by SaD-I and SaD-II hosted in ReD. Note that stylolite (St) crosscut the different dolomite types.

5.2 Late calcite types

Different calcite types have been found spatially related to stratabound and patchy dolostones. Brown calcite (BrC) shows poorly packed equigranular anhedral crystals with very fine sizes. They occur as: i) non-selective replacement of SuD, preserving the rhombohedral morphology; and ii) selective replacement along crystallographic planes of SaD-II (Fig. 8f). White calcite (WhC) is densely packed, with medium to very coarse euhedral to subhedral crystals (100µm) They occur as blocky cement without any preferred orientation along veinlets associated with breccias showing bright red luminescence (Figs. 8d and 8e). Yellow calcite (YeC) consists of large druses (centimetric to decimetric) in vuggs and fractures in dolomite bodies and limestones (Fig. 8g).

5.3 Zn-(Fe-Pb) minerals

Zn-(Fe-Pb) mineralization is associated with the dolomitized interval of the Upper Member of Puerto Lorente Fm. Two deposit-types have been distinguished: i) hypogene Zn-(Fe-Pb) sulfide ores consisting of marcasite, sphalerite (Fig. 8h) and minor galena; and ii) secondary Zn-(Fe-Pb) non-sulfide mineralization ("calamine" deposits) mainly consisting of smithsonite, cerussite and goethite. The relationship with dolomitization,

and the morphology and mineralogy of the primary mineralization corresponds to a Mississippi Valley-Type (MVT) deposit.
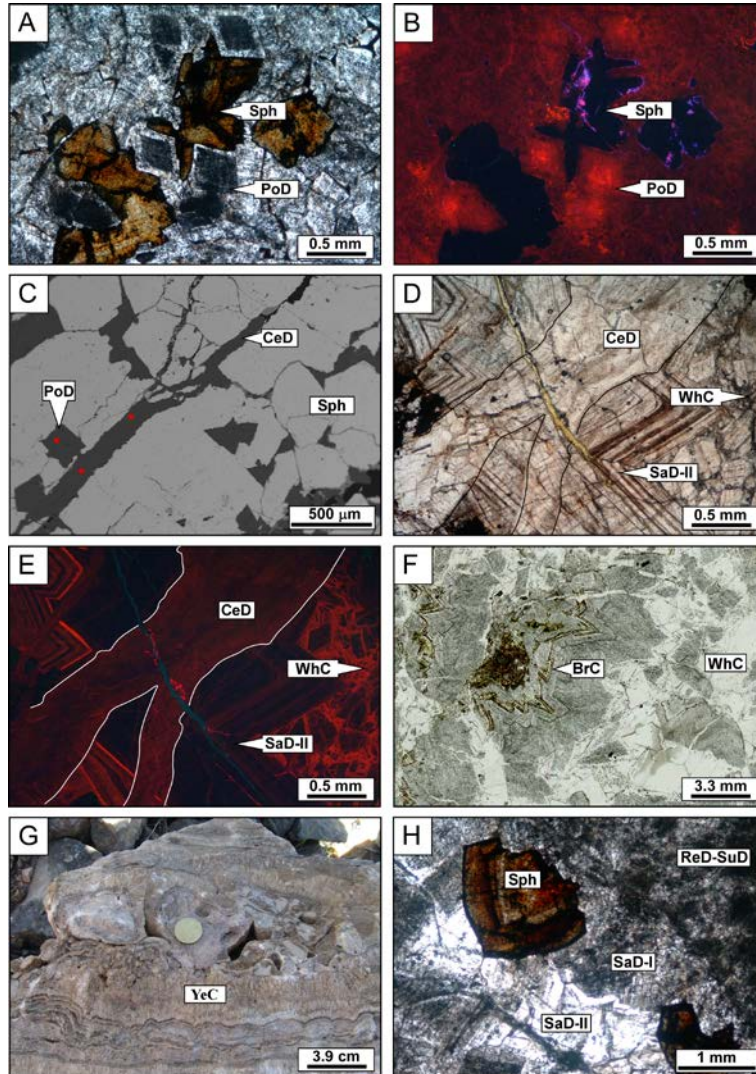

Figure 8. Petrographic characteristics of late dolomite and calcite types, as well as Zn ores. (A) Transmitted light (TL) microphotograph of PoD replacing sphalerite crystals. (B) Cathodoluminescence (CL) image of PoD showing bright red luminescence nucleus. (C) SEM backscattered image of PoD replacing sphalerite and CeD filling fractures. Red points mark the position of the electron microprobe analyses. (D) CeD infilling fractures crosscutting SaD-II (WhC: white calcite) (TL). (E) Dull patchy red luminescence of CeD (CL). (F) Brown calcite (BrC) along microfractures and cleavage

in saddle dolomite and with calcite (WhC) infilling fractures and conforming breccciation zones. (G) Field observation of yellow calcite druses in fracture zones affecting fine replacive dolomite. (H) Sphalerite (Sph) crystals post-dating SaD-I and pre-dating SaD-II (TL).

6 Analytical results

The different carbonate phases were analyzed for their elemental and isotopic (C, O and Sr) composition. Results are summarized in Table 1.

6.1 Dolomite element composition

One hundred and eight analyses of major and minor elements of dolomites (MgO, CaO, FeO, ZnO, Na_2O, SrO) were performed. The different dolomite types show similar MgO contents ranging from 18.46 to 24.12 wt.%, CaO values between 28.59 and 32.28 wt.% and Mg/Ca ratios within a 0.82 to 1.09 range (Table 1). However, matrix-replacive (ReD) as well as ore-replacive (PoD) dolomite crystals have most restricted stoichiometry values between 48.86 to 50.15 mol% and 49.14 to 52.68 mol% $CaCO_3$ respectively, whereas dolomite cements (SuD, SaD and CeD) show more variable mol% $CaCO_3$ values between 45.59 to 53.98 (Table 1, Fig. 9).

Differences between each dolomite types are observed in the FeO and ZnO contents. Replacive dolomites (ReD and PoD) show FeO contents below 1.93 and 1.70 wt.% respectively, whereas dolomite cements (SuD, SaD and CeD) have a FeO content up to 3.89 wt.% (Table 1, Fig. 9). These relative Fe-enrichments of more than 1 wt.% are consistent with the slightly blue to dark blue colors observed when treated with K-ferricyanide (e.g. Morrow, 1990).

Table 1. Elemental and isotopic geochemistry of carbonate phases.

Phase[a]	MgO	CaO	FeO	ZnO	Na$_2$O	SrO	Mg/Ca	MgCO$_3$	CaCO$_3$	FeCO$_3$	δ^{13}C	δ^{18}O	δ^{18}O	^{87}Sr/^{86}Sr
	(wt. %)				(ppm)			(mol%)			(PDB)	(SMOW)	(PDB)	
Host-L														
n	-	-	-	-	-	-	-	-	-	-	8	8	8	2
Min.	-	-	-	-	-	-	-	-	-	-	+0.5	+27.7	-3.2	0.70723
Mean	-	-	-	-	-	-	-	-	-	-	+2.4	+28.1	-2.7	0.70727
Max.	-	-	-	-	-	-	-	-	-	-	+3.2	+30.9	+0.0	0.70731
St. dv.	-	-	-	-	-	-	-	-	-	-	0.8	1.1	1.1	0.00006
ReD														
n	11	11	11	11	11	2	11	11	11	11	19	19	19	3
Min.	20.07	28.59	0.21	0.00	0.00	46.00	0.91	47.26	48.86	0.28	+0.0	+25.4	-5.3	0.70743
Mean	20.78	29.57	0.90	0.09	139.09	57.00	0.98	48.86	49.96	1.18	+0.3	+26.1	-4.6	0.70755
Max.	21.15	30.85	1.93	0.30	420.00	68.00	1.03	50.15	52.04	2.54	+0.6	+27.0	-3.8	0.70773
St. dv.	0.35	0.73	0.47	0.11	180.64	15.56	0.04	0.89	1.13	0.61	0.2	0.4	0.4	0.00016
SuD														
n	10	10	10	10	10	4	10	10	10	10	46	46	46	8
Min.	19.95	29.00	0.00	0.00	0.00	31.00	0.92	47.86	45.59	0.00	-2.3	+25.1	-5.7	0.70736
Mean	21.20	29.71	1.00	0.08	105.30	39.00	0.99	49.17	49.58	1.25	-0.4	+25.9	-4.8	0.70744
Max.	24.12	30.67	3.89	0.52	363.00	53.00	1.09	50.14	52.14	4.51	+0.9	+27.1	-3.7	0.70763
St. dv.	1.11	0.56	1.18	0.16	130.55	10.46	0.05	0.74	1.69	1.38	0.5	0.5	0.5	0.00008
SaD														
n	50	50	50	50	50	10	50	50	50	50	32	32	32	14
Min.	18.46	29.06	0.00	0.00	0.00	39.00	0.82	43.65	48.69	0.00	-0.4	+25.2	-5.6	0.70741
Mean	20.42	30.28	0.90	0.14	201.20	47.60	0.94	47.84	50.99	1.18	+0.1	+26.4	-4.4	0.70769
Max.	21.52	32.28	2.95	1.15	750.00	63.00	1.02	50.37	53.98	3.96	+0.8	+27.6	-3.2	0.70830
St. dv.	0.74	0.87	0.87	0.26	205.10	7.92	0.05	1.57	1.50	1.15	0.3	0.6	0.6	0.00028
PoD														
n	17	17	17	17	17	-	17	17	17	17	-	-	-	-
Min.	19.21	29.21	0.16	0.00	0.00	-	0.87	45.69	49.14	0.20	-	-	-	-
Mean	20.58	30.71	1.16	0.26	204.71	-	0.93	47.52	50.97	1.51	-	-	-	-
Max.	21.52	31.59	1.70	1.03	620.00	-	1.01	49.64	52.68	2.21	-	-	-	-
St. dv.	0.60	0.59	0.38	0.26	186.12	-	0.04	1.03	0.89	0.50	-	-	-	-
CeD														
n	4	4	4	4	4	-	4	4	4	4	-	-	-	-
Min.	19.35	28.81	1.00	0.03	0.00	-	0.87	45.22	48.93	1.30	-	-	-	-
Mean	20.23	29.72	1.82	0.33	180.00	-	0.95	47.46	50.13	2.41	-	-	-	-
Max.	21.56	30.97	2.22	0.62	330.00	-	1.02	49.78	52.00	2.95	-	-	-	-
St. dv.	0.97	0.90	0.56	0.33	145.83	-	0.06	1.98	1.41	0.75	-	-	-	-
YeC														
n	-	-	-	-	-	-	-	-	-	-	2	2	2	-
Min.	-	-	-	-	-	-	-	-	-	-	-7.3	+23.9	-6.7	-
Mean	-	-	-	-	-	-	-	-	-	-	-7.1	+24.2	-6.3	-
Max.	-	-	-	-	-	-	-	-	-	-	-7.0	+24.4	-6.5	-
St. dv.	-	-	-	-	-	-	-	-	-	-	0.2	0.3	0.3	-

[a]*Host-L*: host limestone; *ReD*: matrix-replacive dolomite; *SuD*: sucrosic dolomite cement; *SaD*: saddle dolomite cement; *PoD*: ore-replacive porphyrotopic dolomite; *CeD*: cement dolomite cement; *YeC*: yellow calcite; *n*: number of analyses; Min.: minimum value; Mean: mean value; Max.: maximum value; St. dv.: standard deviation.

ReD, SuD and CeD are non-zincian dolomites with ZnO contents below 0.62 wt.%, whereas SaD and PoD phases are more zincian, with ZnO contents up to 1.15 wt.% (Table 1). This enrichment in Zn is consistent with SaD being intimately related to sphalerite precipitation. As PoD replaces sphalerite, it may capture variable amounts of Zn, which may cause its untypical marked pleochroism. Na content in the different dolomite phases is lower than 750 ppm and Sr content in ReD, SuD and SaD dolomite types is within a 31 to 68 ppm range (Table 1).
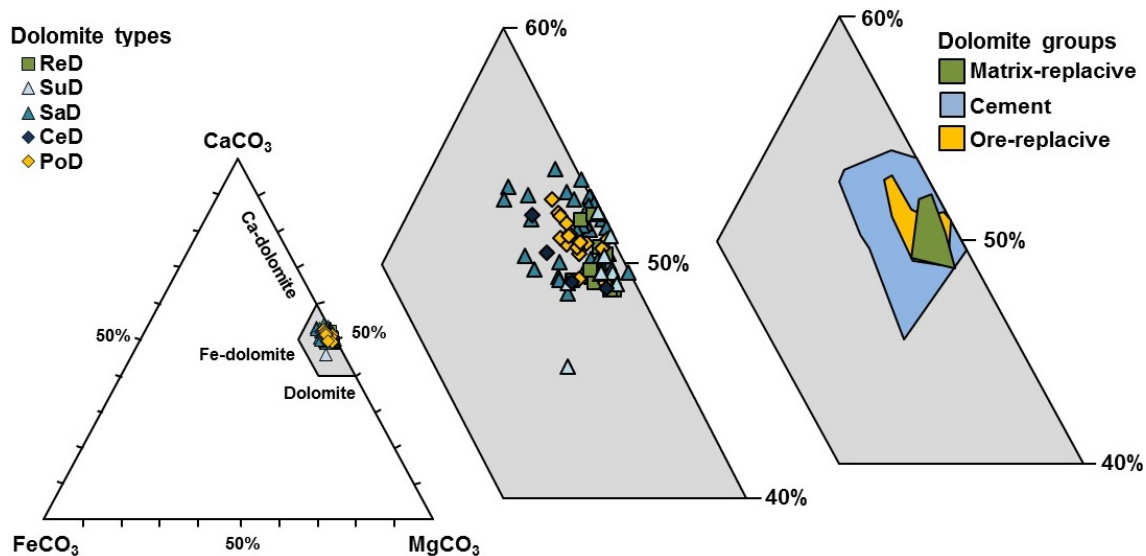
Figure 9. CaCO$_3$-MgCO$_3$-FeCO$_3$ ternary plot showing the composition obtained from electron microprobe analyses of matrix-replacive dolomites (ReD), sucrosic (SuD), saddle (SaD) and planar-e (CeD) dolomite cements, and ore-replacive porphyrotopic dolomite (PoD).

6.2   Carbon and Oxygen isotopes

One hundred and seven samples of host limestones, dolomites and calcites were analyzed for their carbon and oxygen isotope composition (Table 1, Fig. 10). Host limestones (Middle Mb of Sierra del Pozo and Cerro Lobo Fms) show $\delta^{13}C_{V-PDB}$ and $\delta^{18}O_{V-SMOW}$ values between +0.5 to +3.2‰ and from +27.6 to +30.9‰ respectively (Table 1). These values are compatible with carbonates precipitated from Upper Jurassic to Early Cretaceous seawater (Veizer et al., 1999) (Fig. 10).

Matrix-replacive (ReD) and cement (SuD and SaD) dolomites shows similar C and O isotope values ($\delta^{13}C_{V-PDB}$: -2.3 to +0.8‰; $\delta^{18}O_{V-SMOW}$: +25.1 to +27.6‰), which overlap each other, although ReD dolomite shows more restricted C isotope values ($\delta^{13}C_{V-PDB}$: +0.0 to +0.6 ‰) than cement dolomites (Table 1, Fig. 10). The late dolomite

crystals (PoD and CeD) were not possible to analyze due to their small grain size. $\delta^{13}C$ and $\delta^{18}O$ values of dolomites are lower than those of the host limestones, showing a difference of 5‰ for carbon and 3‰ for oxygen approximately.

YeC is the only calcite type analyzed, showing $\delta^{13}C_{V-PDB}$ values from -7.3 to -7.0‰ and $\delta^{18}O_{V-SMOW}$ of +23.9 to +24.4‰ (Table 1). Although $\delta^{18}O$ values are similar, $\delta^{13}C$ values are clearly lower than those of dolomites, showing a ^{12}C enrichment (Fig. 10).

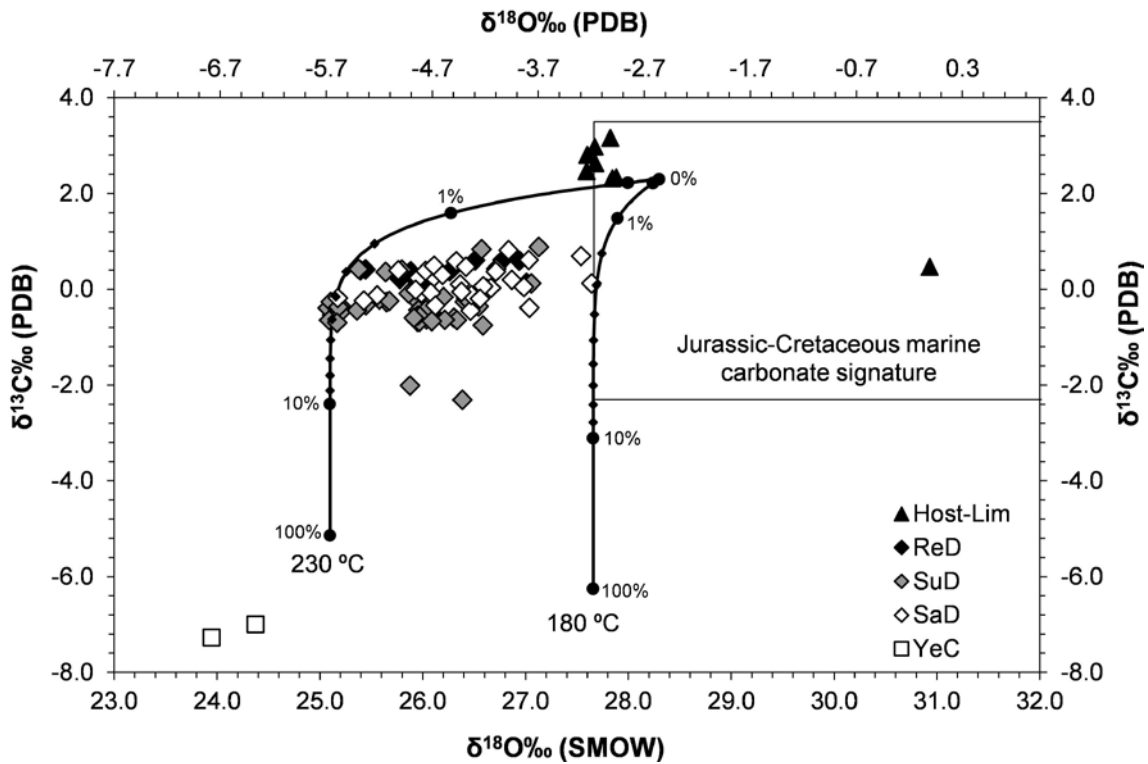Figure 10. $\delta^{13}C$ vs $\delta^{18}O$ cross-plot of host limestone (Host-Lim), matrix-replacive dolomite (ReD), sucrosic dolomite cement (SuD), saddle dolomite cement (SaD), and yellow calcite cement (YeC). Box indicates the range of Jurassic to Cretaceous marine carbonate according to Veizer et al. (1999). C-O isotope model curves were calculated in terms of fluid-rock interaction for dolomite (continuous dark coarse lines) at temperatures of 230ºC and 180ºC (see: Zheng and Hoefs, 1993).

26

6.3   Strontium isotopes

Twenty seven samples of host limestones and dolomites were analyzed for their strontium isotope composition (Table 1). The Cerro Lobo Fm host limestone has a $^{87}Sr/^{86}Sr$ ratio of 0.70723 to 0.70731, falling within the range of the Upper Jurassic to Early Cretaceous marine carbonate values (Fig. 11a) (Veizer et al., 1999). $^{87}Sr/^{86}Sr$ ratio varies from 0.70743 to 0.70773 in ReD and from 0.70736 and 0.70763 in SuD dolomite. SaD dolomite have slightly higher ratio, ranging from 0.70741 to 0.70830 (Table 1, Fig. 11a). In general, most dolomite types have relatively low Sr concentrations (31-68 ppm; see Table 1) and $^{87}Sr/^{86}Sr$ ratios close to the reported Upper Jurassic to Early Cretaceous seawater values (Fig. 11b).
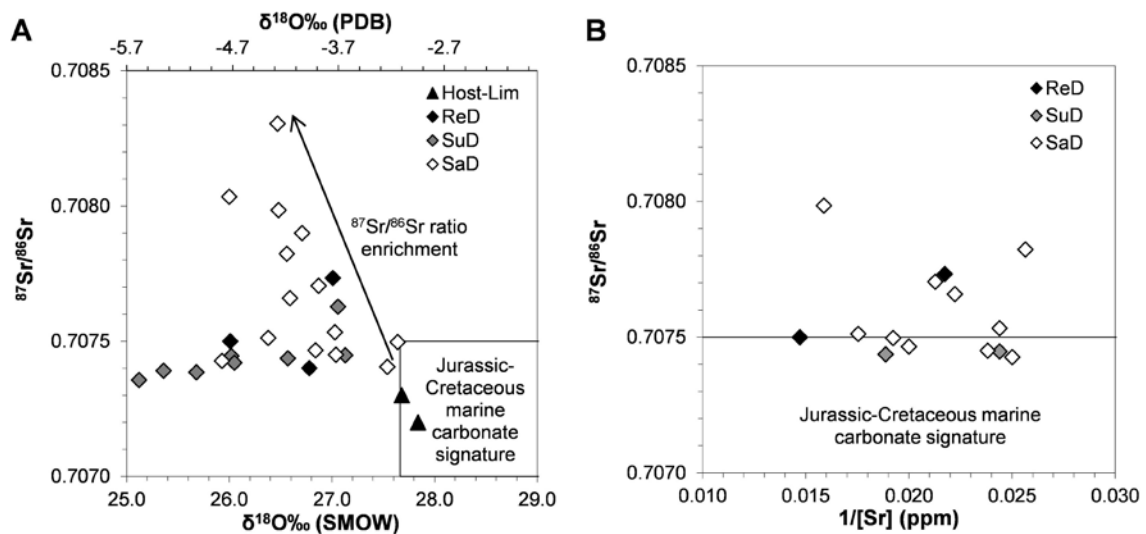

Figure 11. (A) $\delta^{18}O$ and $^{87}Sr/^{86}Sr$ plots of host limestone (Host-Lim), matrix-replacive dolomite (ReD), sucrosic dolomite cement (SuD) and saddle dolomite cement (SaD). Box indicates Middle Jurassic to Lower Cretaceous marine carbonate according to Veizer et al. (1999). (B) $^{87}Sr/^{86}Sr$ vs. 1/[Sr] cross-plot for ReD, SuD and SaD dolomites.

7   Fluid inclusion microthermometry

7.1   Petrography

Four fluid inclusion populations (FIPs) have been identified in dolomite and sphalerite crystals: i) two-phase liquid and vapor; ii) mono-phase liquid; iii) two-phase hydrocarbon and vapor; and iv) mono-phase hydrocarbon. The two-phase liquid and vapor FIPs at room temperatures have been found in crystal cores of matrix-replacive ReD-I to ReD-II dolomite transition type (Fig. 12a), in concentric growth-zones of SuD, SaD-II and PoD dolomites (Figs. 12b and 12d) and throughout individual crystals of SaD-I and sphalerite (Figs. 12c and 12e) pointing to primary origin. These FIPs are irregular to elongate in shape with sizes ranging from 3 to 15 µm and variable vapor/liquid ratios (5 to 25). No microthermometrical measurements in SuD and PoD dolomites could be performed due the small size (commonly less than 5 µm) and scarcity of the inclusions. Also, CeD dolomite is free of FIPs.

Single-phase FIP's show regular to irregular shapes and sizes ranging from 3 up to 50 µm. Some of these mono-phase FIPs are related with two-phase fluid and vapor fluid inclusion populations (3 to 25 µm in size) in the same growth-planes showing evidences of necking. Consequently, these two-phase FIPs are discarded for homogenization temperature measurements. Also, necking is identified by the high variability of vapor/liquid ratios, shapes and sizes of two-phase fluid and vapor FIPs. On the other hand, mono-phase liquid FIPs have been recognized with large lensoid forms and sizes up to 50 µm cross-cutting the different inclusion populations and pointing to a secondary origin.
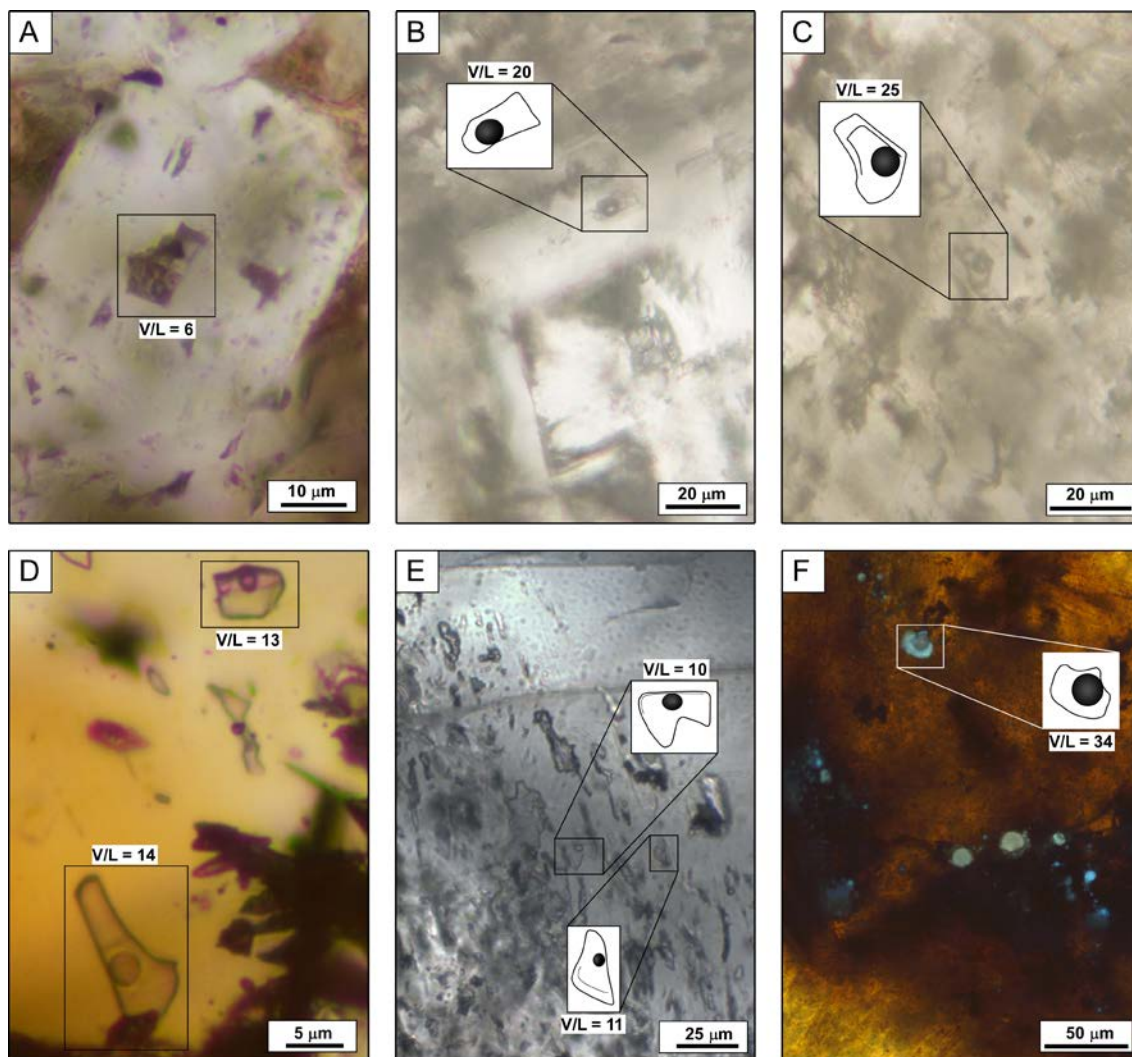
Figure 12. Petrographic characteristics of two-phase fluid inclusions (liquid + vapor) from: (A) matrix-replacive planar-s to planar-e dolomite transition (ReD-I/ReD-II); (B) sucrosic dolomite cement (SuD); (C) grey saddle dolomite cement (SaD-I); (D) sphalerite (Sph); and (E) milky white to pinkish saddle dolomite cement (SaD-II). (F) Blue fluorescent oil fluid inclusions from sphalerite (combined transmitted (TL) and ultraviolet (UV) 365 nm light).

Two-phase hydrocarbon and vapor and mono-phase oil FIPs occur in sphalerite crystals as rounded inclusions with sizes ranging from 1 to 25 µm and high vapor/liquid ratios (>25) (Fig. 12f). This FIP always has been observed related to small fractures, and therefore, pointing to secondary origin. Hydrocarbon bearing FIPs show blue

fluorescence under UV light and brown color under plane polarized light. No microthermometric measurements were performed on two-phase hydrocarbon and vapor FIPs.

7.2   Microthermometric results

Results of microthermometrical analyses from two-phase liquid and vapor FIPs are summarized in Table 2. In heating runs, four temperatures were recorded: i) the eutectic temperature (T_e); ii) the hydrohalite-melting temperature ($T_{m,hydrate}$); iii) the last ice-melting temperature ($T_{m,ice}$); and iv) the homogenization temperature (T_e). No pressure correction was applied to the T_e from fluid inclusion measurements, as the depth of burial at the time of dolomitization is unknown.

The T_e was observed in fluid inclusions in ReD-I/ReD-II (n=3), SaD-I (n=1), SaD-II (n=11) dolomites and sphalerite (n=11), occurring at temperatures between -64.5 and -40.6°C with average temperature of -51.1°C. These temperatures are close to the eutectic of the H_2O-NaCl-$CaCl_2$ (T_e: -52°C) and the H_2O-NaCl-$CaCl_2$-$MgCl_2$ (T_e: -57°C) systems (Davis et al., 1990). The hydrohalite-melting (NaCl·$2H_2O$) was measured in fluid inclusions in different dolomite types and sphalerite showing temperatures ranging between -24.9 and -21.0°C with an average temperature of -22.3°C. $T_{m,ice}$ values in different dolomite types and sphalerite crystals ranged from -25.5 to -2.8°C (n=80) with two modes at -24.5 and -5.5°C (Table 2, Fig. 13a): ReD-I/ReD-II, -10.3 to -5.7°C (n=11); SaD-I, -5.4 to -2.8°C (n=10); sphalerite, -25.5 to -5.4°C (n=31); and SaD-II, -24.6 to -2.7°C (n=28). Modelling these data in the H_2O-NaCl-$CaCl_2$ system yields estimated bulk salinities of 4.7-25.2 wt.% NaCl+$CaCl_2$, with 20.2-4.0 wt.% NaCl and 11.3-0.7 wt.% $CaCl_2$.

Table 2. Fluid inclusion data for dolomites and sphalerite samples from the Riópar area.

Phase[a]	T_E	$T_{M, HYDRATE}$	$T_{M,ICE}$	T_H	NaCl+CaCl$_2$	NaCl	CaCl$_2$
	(°C)[b]				(wt.%)		
ReD-I/ReD-II							
n	3	1	11	24	11	11	11
Min.	-59.3	-	-10.3	185.9	9.1	7.7	1.4
Mean	-51.5	-21.4	-7.5	216.4	11.2	9.6	1.7
Max.	-45.1	-	-5.7	240.3	13.7	11.6	2.0
St. dv.	7.2	-	1.5	17.4	1.7	1.5	0.3
Mode	-	-	-6.5	205; 235	10.5	8.5	1.5
SaD-I							
n	1	1	10	32	10	10	10
Min.	-	-	-5.4	177.0	4.8	4.1	0.7
Mean	-50.3	-21.4	-4.4	216.1	7.2	6.1	1.1
Max.	-	-	-2.8	246.6	8.7	7.4	1.3
St. dv.	-	-	0.8	19.2	1.2	1.0	0.2
Mode	-	-	-4.5	235	7.5	6.5	1.5
Sph							
n	11	9	31	39	31	31	31
Min.	-64.5	-24.9	-25.5	150.1	8.7	7.4	1.3
Mean	-51.6	-22.4	-17.8	198.6	19.8	14.9	4.0
Max.	-45.9	-21.0	-5.4	240.6	25.2	20.2	11.3
St. dv.	6.25	1.1	7.1	25.62	5.6	3.4	3.3
Mode	-49.5	-21.5	-10.5; -24.5	210	14.5; 24.5	16.5	2.5; 8.5
SaD-II							
n	11	6	28	38	28	28	28
Min.	-60.2	-24.3	-24.6	156.5	4.7	4.0	0.7
Mean	-50.9	-22.6	-9.0	208.6	11.8	9.8	2.1
Max.	-40.6	-21.2	-2.7	248.8	24.8	19.8	9.4
St. dv.	4.6	1.4	6.9	19.8	6.3	4.9	1.8
Mode	-49.5	-21.5	-5.5; -21.5	195; 225	8.5	7.5	1.5

[a] *ReD-I/ReD-II*: matrix-replacive planar-s to planar-e dolomite transition; *SaD-I*: grey saddle dolomite cement; *Sph*: sphalerite; *SaD-II*: milky to pinkish saddle dolomite cement; *n*: number of analyses; Min.: minimum value; Mean: mean value; Max.: maximum value; St. dv.: standard deviation; Mode: mode value.
[b] T_E: eutectic temperature; $T_{M,HYDRATE}$: hydrohalite melting temperature; $T_{M,ICE}$: ice melting temperature; T_H: homogenization temperature.

T_h data, measured in fluid inclusions from ReD-I/ReD-II, SaD-I, SaD-II dolomites and sphalerite fall in the 150.1 to 248.8°C range (*n*=133) showing a normal Gaussian distribution with the mode at 205°C (*n*=25) (Table 2, Fig. 13b). In ReD-I/ReD-II dolomite, T_h values range from 185.9 to 240.3°C (*n*=24). 79% of T_h data fall in a 205 to 235°C range. T_h histogram of ReD-I/ReD-II shows two modes at 205 and 235°C. In SaD-I, T_h data range from 177.0 to 246.6°C (*n*=32) with a mode at 235°C and 81% of measured data is in a 195 to 235°C range. T_h in sphalerite is quite variable, ranging from 150.1 to 240.6°C (*n*=39) with a mode at 210°C and 74% of measured data fall in the range of 185 to 235°C. In SaD-II, T_h data is observed in the range of 156.5 to 248.8°C (*n*=38) and 84% of all T_h values are between 195 and 235°C. The T_h frequency histogram shows two well-defined modes at 195 and 225°C. The T_h-salinity plot (Fig.

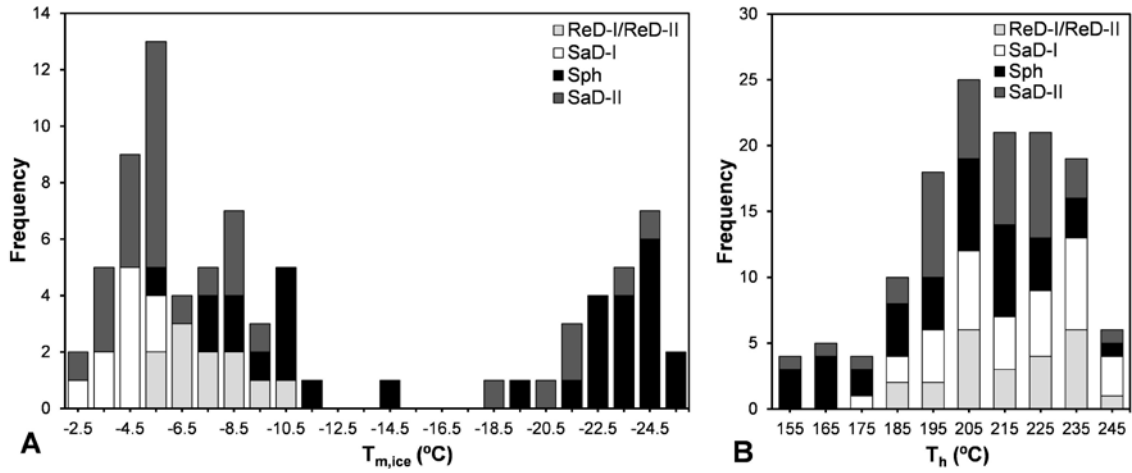14) points to the presence of two groups of data of different salinity but with a similar T_h spread.

Figure 13. Frequency histograms showing distribution of: (A) melting ice temperature ($T_{m,ice}$) and (B) homogenization temperatures (T_h) from different dolomite types (ReD-I/ReD-II, SaD-I and SaD-II) and sphalerite (Sph).
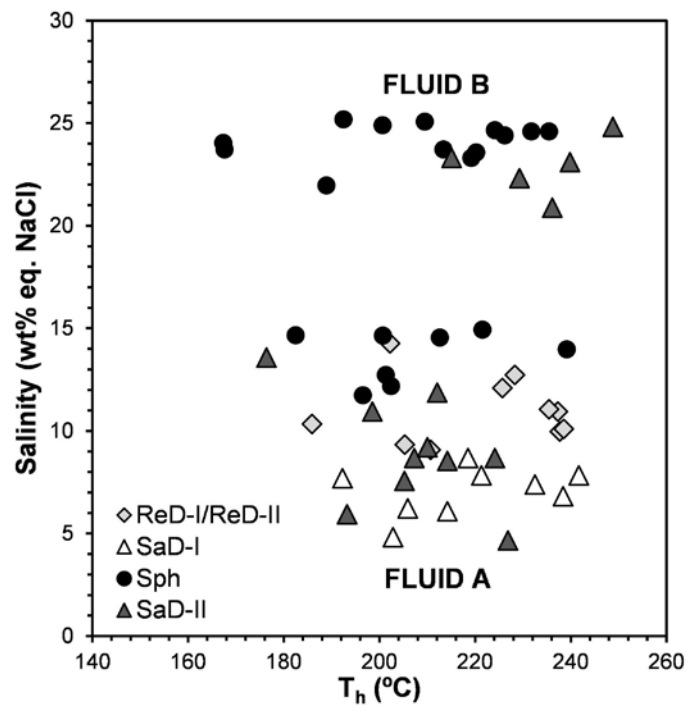

Figure 14. Salinity *vs* homogenization temperature cross-plot from different dolomite types (ReD-I/ReD-II, SaD-I, SaD-II) and sphalerite (Sph).

8   Discussion

8.1   Paragenetic sequence

The deposition of Upper Jurassic to Lower Cretaceous slope carbonatic sediments, with a minor terrigenous component, occurred in a marine environment. Micrite envelops and calcite cements (Fig 6c) must have developed as early diagenetic products of the formed limestone; grain component dissolution (ooids and orbitolinids: Figs. 5c and 6a) and stylolite formation (Figs. 6h and 15) also occurred previous to dolomitization. Fracturing (San Jorge-Socovos system) must have been coeval to sedimentation and/or diagenesis during the rifting stage (Figs 3, 4 and 15).

Matrix-replacive dolomites are interpreted to be the initial stage of dolomitization as indicated by: i) the coexisting of ReD-I with ReD-II dolomites replacing grains and bioclasts of the precursor limestone observed as ghosts (Figs. 6a and 6b); ii) the preserved moldic porosity from ooids and orbitolinids (Figs. 5b, 6a and 6b); and iii) the presence of ReD-II dolomites replacing micritic components of host-limestones (Fig. 6c).

The occurrence of ReD dolomite ghosts in the core of dolomite SuD crystal cements indicates a neomorphic recrystallization (Figs. 6d and 6e) which post-dated matrix-replacive dolomite (Fig. 15). The porosity thus created together with a new fracturing event after SuD formation (Fig. 15) could have created new dolomitizing and mineralizing fluid-flow pathways; they allowed the formation of additional porosity and void-filling dolomitization producing saddle dolomite cements (SaD) and hypogenic Zn-(Fe-Pb) ore (Figs. 7, 9g and 15). The coarse crystallinity of saddle dolomite cements is typical of burial dolomitization (Gregg and Sibley, 1984).

33

During a later pulse of dolomite precipitation sphalerite was replaced by planar-e porphyrotopic dolomite (PoD: Figs. 8 and 15). Another fracturing event could have facilitated the last dolomitizing fluid pulse which was responsible for the precipitation of planar-s cements (CeD: Fig. 8 and 15). A late episode of calcitization, which includes dolomite-replacive calcite (BrC) and cements in fractures that cross cuts the previous phases (WhC and YeC) post-dated all dolomites (Figs. 8 and 15).
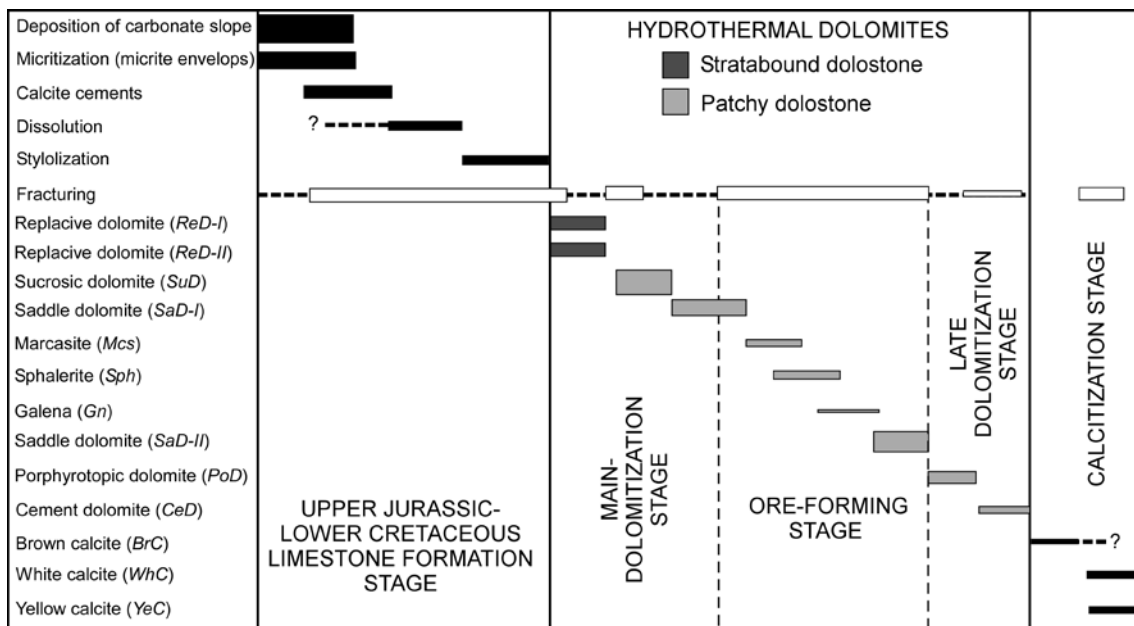

Figure 15. Summary of the paragenetic succession in the Riópar dolomitized limestones related to Zn-(Fe-Pb) ores, as recognized from detailed conventional and cathodoluminescence petrography. The diverse fracturing events are represented along a single line.

8.2   Controls of dolomitization and mineralization

Matrix replacive planar-s and planar-e dolomites (ReD-I, ReD-II and transitions between them) only affect the Lower and Upper Mb of Sierra de Pozo Fm (stratabound dolostone: Fig. 4); this observation suggests some physical (e.g. permeability, porosity,

size of particles) and chemical controls (e.g. mineralogy) of the precursor limestone. However, dolomite cements and ore-replacive dolomites occur in all strata from the Lower Mb of Sierra de Pozo Fm up to Arroyo de los Anchos Fm (patchy geobodies: Fig. 4), which indicates they formed without any apparent lithological/facies control.

Patchy dolostone and Zn ore deposits appear nearer the San Jorge fault than Socovos fault (Fig. 4). Therefore, the contribution of the dolomitization fluid from the Socovos fault must have been low to moderate, in contrast with the influx of dolomitizing fluid from San Jorge fault, indicating a structurally-controlled fluid circulation. Although the relationship of stratabound dolostones with San Jorge fault is unclear, the similar element compositions, C and O isotopic signatures and T_h's of two-phase FIPs (Table 1 and Figs. 9, 10 and 14) of matrix-replacive and cement dolomites as well as sphalerite crystals suggest a genetic relationship between stratabound and patchy dolomitization and mineralization. Consequently, stratabound dolostones are also (partially) fault-controlled, supporting the idea of a single and continuous dolomitizing process which was developed through different pulses (e.g. Merino and Canals, 2011).

The shapes and crosscutting relationships of the dolomite bodies and host limestones (Figs. 4) suggest a late diagenetic origin for the Riópar dolomitization. Late burial diagenetic dolomites typically contain only a few hundred ppm Na (Gasparrini et al., 2006) and tend to have lower Na contents than early diagenetic ones (Brand and Veizer, 1980). However, late diagenetic dolomites generally have lower Sr concentration than early diagenetic dolomites (Brand and Veizer, 1980; Gasparrini et al., 2006). Therefore, the low Na and Sr contents measured in matrix-replacive and cement dolomites (Table 1) may confirm a late burial origin for the dolomitizing process. Besides, their $\delta^{18}O$ depletion (Table 1 and Fig.10) is comparable with that of

late burial dolomites reported in the literature (e.g. Boni et al., 2000; Gasparrini et al., 2006).

8.3   Evidence of hydrothermal dolomitization

A subsidence analysis performed by Hanne et al. (2003) in the Prebetic Zones (Río Segura-GI, Elche de la Sierra and Batán del Puerto, Fig. 1) resulted in a maximum total depth for the Mesozoic sequence after Cretaceous rifting of around 2200 m. The maximum temperature reached by Mesozoic rocks due to this burial depth would have been less than 100ºC using a maximum geothermal gradient of rifting scenarios of 45ºC/km. On the other hand, this maximum temperature for burial is consistent with vitrinite reflectance values from Albian sandstones (Utrillas Fm), taken in the Socovos-2 borehole (SE of the studied area: Fig. 1), that are below Ro=0.5%, implying a maximum temperature lower than 70-80ºC during the post-depositional evolution (Barbero et al., 2001). Moreover, apatite fission-track thermal model analysis from Cretaceous samples of the Sierra de Segura and Sierra de Cazorla (Fig. 1) indicate that the post-depositional thermal evolution attained temperatures not exceeding 70-80ºC for most of the Late Cretaceous and Tertiary rocks (Barbero and López-Garrido, 2006).

However, the T_h values obtained in the studied dolomites and sphalerite (mode at 205ºC: Fig. 14) indicate that the stratabound, patchy dolomitization and related ore occurred at higher temperatures than those reached by the burial of host carbonates. Consequently, these dolomites must have generated by hydrothermal process, which requires an alternative heat source or depth for the dolomitizing fluids.

8.4   Origin of the fluids

The C and O isotopic distribution of studied dolostones depicts a horizontal trend with a small $\delta^{18}O$ ($\approx$ 3.5‰) and $\delta^{13}C$ ($\approx$ 2‰) shift. Compared to the regional limestone isotopic values the dolostones show a relatively depleted $\delta^{18}O$ and $\delta^{13}C$ values (Fig. 10). This distribution can be explained by an interaction of hydrothermal fluids with the regional marine limestones of Upper Jurassic to Lower Cretaceous ages. Assuming an open system and using the equations of Zheng and Hoefs (1993), dolomite isotope data is consistent with the interaction between fluids with a CO_2 content of 0.1M and an initial isotopic composition of $\delta^{13}C$ = -8‰ and $\delta^{18}O$ = +17.0‰ and the host limestones having a $\delta^{13}C$ = +2.3‰ and a $\delta^{18}O$ = +28.3‰ at a temperature range between 180 and 230°C (Fig. 10). The carbon dominant species in the fluid was assumed to be H_2CO_3. Fractionation equation between water and dolomite was taken from Land (1983) and between H_2CO_3 and dolomite from Chacko et al. (1991). It is interesting to notice that the dolomitizing fluids are isotopically enriched in ^{18}O. Such isotopic composition ($\delta^{18}O$ $\approx$ +17.0‰), can be achieved by a low $\delta^{18}O$ fluid (i.e. meteoric, evaporated seawater) after isotopic equilibration with carbonates. The high salinities measured in FI and the absence of igneous events in the Riópar area, suggests that dolomitizing fluids could originally be either evaporated seawater that circulated through carbonated aquifers, and then, became enriched in ^{18}O and/or probably acquiring a high salinity from dissolution of Triassic evaporites.

The assumed $\delta^{13}C$ value for the dolomitizing fluid ($\approx$ -8‰) indicates a carbon source related to organic matter. The presence of hydrocarbon-bearing FIPs is consistent with the ^{13}C-depleted isotopic source, although the spatial relationship of this FIP with sphalerite crystals suggests the presence of hydrocarbons after the Zn-(Fe-Pb) ore-forming stage (Fig. 12f). However, the narrow $\delta^{13}C$ range of hydrothermal dolomites,

close to the original marine signature of the host limestones, indicates that the carbon isotopic composition of the fluid was buffered by the host rock.

Therefore, the observed O-shift of dolomites could be explained through a temperature decrease ($\approx 40°C$) during dolomitization of host limestones. The small C-shifts of dolomites are consistent with this hypothesis, as the carbon isotopic variations of carbonates are less temperature dependent. In any case, $\delta^{13}C$ and $\delta^{18}O$ values of dolomites indicate that the interaction took place at low fluid/rock ratios, suggesting that dolomitizing fluids flowed through high permeability lithological units.

The similar eutectic temperatures found in fluid inclusions from different dolomite phases and sphalerite, suggest the presence of a single $NaCl$-$CaCl_2$-bearing (with minor $MgCl_2$) fluid type. Moreover, dolomites and sphalerite precipitated at a similar T range, pointing to a temperature equilibration of the system, either at the precipitation site or at the fluid source area. The spread of T_h values obtained might be related to recrystallization, necking or stretching phenomena. However, a model temperature of 180 to 230ºC explains the $\delta^{18}O$ variation of the different dolomite phases (Table 1, Fig. 10), which suggests that the temperature during dolomitization ranged between 180 and 230ºC. Moreover, the warm fluid depicts two differentiated salinity groups of data which could be interpreted as the contribution of two end member fluids: a fluid of low salinity (fluid A, around or less than 5 wt.% eq. NaCl) and a higher salinity brine (fluid B, around or more than 25 wt.% eq. NaCl) (Fig. 14). The presence of single-phase aqueous fluid inclusions are indicative of fluid trapping at temperatures of less than 50ºC (Goldstein and Reynolds, 1994). Therefore, we cannot rule out the presence of another cold and probably diluted fluid involved in the dolomitization and mineralization stages. In any case, such T_e-$T_{m,ice}$-T_h distribution may be explained by three different scenarios for the fluid source region. i) A unique hot and saline fluid

type, stagnant for prolonged periods of time which stratifies in two layers of different salinity by gravitational fractionation under isothermal conditions (Bons and Gomez-Rivas, 2013). This possibility requires a thick reservoir, where the uppermost part would contain the moderate-salinity and less dense fluid (fluid A) and the lowermost part would be occupied by the high-salinity and more dense fluid (fluid B). ii) Two fluids at similar temperature (at similar depths) but of different salinities separated by a natural barrier (e.g. impermeable Keuper facies: Figs. 3 and 4), constituting two differentiated reservoirs. iii) Two fluids of contrasting temperature and salinity, one of low-temperature and low-salinity (fluid A) and other of high-temperature and high-salinity (fluid B), which mix and reach an equilibrium temperature preserving their original salinity. The first two possibilities consist of fluids that reach the deposition site already equilibrated in terms of temperature. The later one implies a temperature equilibration on site after certain time. All three cases, though, respond to mixing of fluids at different proportions that has evolved with time.

On the other hand, late yellow calcite (YeC) shows a ^{13}C-depleted values (Fig. 10). They could represent the involvement of waters enriched in soil-derived CO_2 and calcite precipitation in the vadose meteoric environment under near-surface conditions (e.g. Hudson, 1977).

8.5   Evolution of the fluids and precipitation model

The salinity range of fluids trapped in ReD-I/ReD-II and SaD-I dolomites (5 to 14 wt.% eq. NaCl) of the main-dolomitization stage (Fig. 14) might be the result of mixing between a dominant fluid A and minor fluid B ($X_{fluid A} > X_{fluid B}$). $^{87}Sr/^{86}Sr$ isotopic ratios of ReD and SuD dolomite is close to that of limestones of Jurassic to Cretaceous age, although some of data show values which are slightly more radiogenic (Fig. 11),

indicating that the dominated fluid A was isotopically equilibrated with the host-limestones with a minor interaction with Rb-bearing minerals.

On the other hand, the wide salinity range of fluids trapped in sphalerite (9 to 25 wt.% eq. NaCl) and dolomite SaD-II (5 to 25 wt.% eq. NaCl) of the ore stage might be the result of mixing between fluid A and B at different proportions of the two end members fluids, although the mixing trend cannot be recognized from the T_h vs salinity diagram (Fig. 14). Mixing can occur when faults tap different salinity regions of the same stratified aquifer or different aquifers. The Sr and O isotope systematic of saddle dolomites (SaD) depicts a trend relating lower $\delta^{18}O$ with higher $^{87}Sr/^{86}Sr$ values (Fig. 11). This relationship points to an increase of ^{87}Sr in the fluid as the temperature increases (lowering the $\delta^{18}O$ of saddle dolomites), and can suggest a mixing between a higher T and $^{87}Sr/^{86}Sr$ ratio fluid with a fluid of slightly lower T and $^{87}Sr/^{86}Sr$ ratio, although no clear mixing evidences of different Sr sources can be deduced (Fig. 11). As Triassic and Cretaceous siliciclastic rocks occur in the Prebetic Zone, it is likely that the most saline fluid became enriched in ^{87}Sr after circulating and interacting with these sediments.

The precipitation of sulfides (sphalerite, galena, marcasite) with saddle dolomite formation is widely accepted as a result of mixing in the genesis of MVT deposits (e.g. Shelton et al., 1992; Kesler, 1996; Grandia et al., 2003; Corbella et al., 2004; Muchez et al., 2005). In these environments, sulfides usually precipitate after mixing between a sulfur-rich, metal-poor, low to moderate-salinity fluid and a metal-rich, sulfur-poor high-salinity fluid. The main-dolomitizing stage, dominated by fluid A, could not have resulted in sulfide precipitation owing the lack of metals in this fluid. Whereas during the ore-forming stage different mixing proportion with metal-rich fluid B would have resulted in restricted sulfide precipitation and deposits of small tonnages.

40

9   Conclusions

The HTD bodies of Riópar are hosted in an Upper Jurassic to Lower Cretaceous carbonate sequence (Middle Kimmeridgian to Aptian). Mapping and stratigraphic studies revealed two types of dolostone geobodies between the San Jorge and Socovos faults: i) stratabound dolomite morphologies following the bedding out to the Socovos fault, indicating a complementary stratigraphic dolomitization control; and ii) patchy dolomite morphologies associated with Zn-(Fe-Pb) ores in the vicinity of San Jorge fault, indicating a preferential fluid flow along fractures and a structural control for dolomitization and mineralization. Stratabound morphologies are characterized by matrix-replacive planar-s (ReD-I) and planar-e (ReD-II) dolomite types and transitions between them. Patchy morphologies are characterized by: i) planar-e sucrosic dolomite cements (SuD) occurring as recrystallizations of ReD dolomites; ii) non-planar saddle grey dolomite cements (SaD-I) occurring as recrystallizations of SuD and in veins pre-dating Zn-(Fe-Pb) sulfides; iii) non-planar saddle milky to pinkish dolomite cements (SaD-II) associated with hypogene Zn-(Fe-Pb) sulfides (sphalerite, marcasite and galena) in veins; iv) ore-replacive planar-e porphyrotopic dolomite (PoD) that replace the previous phases; and v) planar-s dolomite cements (CeD) filling tiny fractures. Also, late calcite was identified post-dating previous dolomites, probably precipitated under meteoric conditions.

The different dolomite types are characterized by similar major element compositions and similar $\delta^{13}C$ (-2.3 to +0.9‰) and $\delta^{18}O$ (+25.1 to +27.6‰) values, suggesting uniform chemical conditions during the formation of stratabound and patchy dolostones, supporting the idea of a continuous dolomitizing process but with different

41

pulses. The lower Na and Sr contents obtained in different dolomites (<750 ppm Na_2O; <68 ppm SrO) suggests a burial/diagenetic origin for all dolomite types. C and O isotope composition of dolomites may be explained through the interaction of fluids (e.g. seawater, residual brines) between an ^{18}O-enriched fluid (+17‰) at temperatures between 180-230ºC and the enclosing carbonates at low fluid/rock ratios. The Sr isotope results for the main-dolomitization phases (ReD, SuD: 0.70736-0.70773) are close to Jurassic and Cretaceous carbonate isotopic values, whereas the dolomites associated to the ore stage (SaD: 0.70741-0.70830) show more radiogenic values indicating that dolomitizing and mineralizing fluid became enriched in [87]Sr after circulating and interacting with siliciclastic rocks.

The main dolomitising stage (ReD-I/ReD-II and SaD-I) show low to moderate fluid inclusions salinity (5 to 14 wt.% eq. NaCl), whereas the dolomitization related to mineralizing stage (sphalerite and SaD-II) spreads to higher salinity values (5 to 25 wt.% eq. NaCl). These data may respond to a mixing between a low salinity fluid (fluid A, less than 5 wt.% eq. NaCl) and a more saline brine (fluid B, more than 25 wt.% eq. NaCl) at different proportions for both stages. As homogenization temperatures are similar in both stages (T_h mode: 205ºC) and higher than the geothermal gradient temperature at the corresponding depth, the fluid must be of hydrothermal origin and must have equilibrated in terms of temperature, either in the reservoir or at the deposition site. Mixing may occur by faults tapping different aquifers in space and through time. The identified single- and two-phase oil FIPs suggests the presence of hydrocarbons during or after the Zn-(Fe-Pb) ore-forming stage, although no oil accumulation has been reported in the area.

Acknowledgements

References

Arias, C., Masse, J.P., Vilas, L., 1996. Relaciones tectónica-sedimentación en el Aptiense de la Sierra Larga, Jumilla (Murcia). Geogaceta 20(1), 43–47.

Ameen, M.S., Buhidma, I.M., Rahim, Z., 2010. The function of fractures and in-situ stresses in the Khuff reservoir performance, onshore fields, Saudi Arabia. AAPG Bull. 94, 27–60. doi: 10.1306/06160909012

Bakker, R.J., 2003. Package FLUIDS 1. Computer programs for analysis of fluid inclusion data and for modelling bulk fluid properties. Chem. Geol. 194, 3–23. doi: 10.1016/S0009-2541(02)00268-1

Banks, C.J., Warburton, J., 1991. Mid-crustal detachment in the Betic system of southeast Spain. Tectonophysics 191, 275–289. doi: 10.1016/0040-1951(91)90062-W

Barbero, L., López-Garrido, A.C., 2006. Mesozoic thermal history of the Prebetic continental margin (southern Spain): Constraints from apatite fission-track analysis. Tectonophysics 422, 115–128. doi: 10.1016/j.tecto.2006.05.011

Barbero, L., López-Garrido, J.A., García-Hernández, M., Quesada, S., Martínez del Olmo, W., 2001. Evolución termal Mesozoica de la Cuenca Prebética (Sierra de

Segura) inferida mediante análisis de huellas de fisión en apatito: resultados preliminares. Geotemas 3 (2), 155–160.

Boni, M., Parente, G., Bechstädt, T., De Vivo, B., Iannace, A., 2000. Hydrothermal dolomites in SW Sardinia (Italy): Evidence for a widespread late-Variscan fluid flow event. Sediment. Geol. 131, 181–200. doi: 10.1016/S0037-0738(99)00131-1

Bons, P.D., Gomez-Rivas, E., 2013. Gravitational fractionation of isotopes and dissolved components as a first-order process in hydrothermal crustal fluids. Econ. Geol. 108 (5), 1195-1201. doi: 10.2113/econgeo.108.5.1.195

Braithwaite, C.J.R., Rizzi, G., Darke, G., 2004. The geometry and petrogenesis of dolomite hydrocarbon reservoirs: introduction. Geol. Soc. London, Spec. Publ. 235, 1–6. doi: 10.1144/GSL.SP.2004.235.01.01

Brand, U., Veizer, J., 1980. Chemical diagenesis of a multicomponent carbonate system-1: Trace elements. J. Sediment. Res. 50, 1219 –1236. doi: 10.1306/212F7BB7-2B24-11D7-8648000102C1865D

Calvo, J.P., Elízaga, E., López-Martínez, N., Robles, F., Usera, J., 1978. El Mioceno superior continental del Prebético Externo: Evolución del Estrecho Norbético. Boletín Geológico y Minero 89, 407–426.

Chacko, T., Mayeda, T.K., Clayton, R.N., Goldsmith, J.R., 1991. Oxygen and carbon isotope fractionations between CO_2 and calcite. Geochim. Cosmochim. Acta 55, 2867–2882. doi: 10.1016/0016-7037(91)90452-B

Comas, M.C., Platt, J.P., Soto, J.I., Watts, A.B., 1999. The origin and history of the Alboran Basin, insights from ODP Leg 161 results (Western Mediterranean), in Zahn, R., Comas, M.C., and Klaus, A., (Eds.), Proceedings of the Ocean Drilling Program, Texas, Scientific Results: Collage Station 161, pp. 555-580.

Corbella, M., Ayora, C., Cardellach, E., 2004. Hydrothermal mixing, carbonate dissolution and sulfide precipitation in Mississippi Valley-type deposits. Miner. Depos. 39, 344-357. doi: 10.1007/s00126-004-0412-5

Davies, G.R., Smith, L.B., 2006. Structurally controlled hydrothermal dolomite reservoir facies: An overview. Am. Assoc. Pet. Geol. Bull. 90, 1641–1690. doi: 10.1306/05220605164

Davis, D.W., Lowenstein, T.K., Spencer, R.J., 1990. Melting behavior of fluid inclusions in laboratory-grown halite crystals in the systems $NaCl$-H_2O, $NaCl$-KCl-H_2O, $NaCl$-$MgCl_2$-H_2O, and $NaCl$-$CaCl_2$-H_2O. Geochim. Cosmochim. Acta 54, 591–601. doi: 10.1016/0016-7037(90)90355-O

Dewit, J., Foubert, A., El Desouky, H.A., Muchez, P., Hunt, D., Vanhaecke, F., Swennen, R., 2014. Characteristics, genesis and parameters controlling the development of a large stratabound HTD body at Matienzo (Ramales Platform, Basque-Cantabrian Basin, northern Spain). Mar. Pet. Geol. 55, 6–25. doi: 10.1016/j.marpetgeo.2013.12.021

Dickson, J.A.D., 1966. Carbonate identification and genesis as revealed by staining. J. Sediment. Res. 36, 491–505. doi: 10.1306/74d714f6-2b21-11d7-8648000102c1865d

Duggan, J.P., Mountjoy, E.W., Stasiuk, L.D., 2001. Fault-controlled dolomitization at Swan Hills Simonette oil field (Devonian), deep basin west-central Alberta, Canada. Sedimentology 48, 301–323. doi: 10.1046/j.1365-3091.2001.00364.x

García-Hernández, M., López-Garrido, A.C., Rivas, P., Sanz de Galdeano, C., Vera, J.A., 1980. Mesozoic paleogeographic evolution of the external zones of the Betic Cordillera. Geol. Mijnb. 50(2), 155–168.

Gasparrini, M., Bakker, R.J., Bechstadt, T., 2006. Characterization of Dolomitizing Fluids in the Carboniferous of the Cantabrian Zone (NW Spain): A Fluid-Inclusion Study with Cryo-Raman Spectroscopy. J. Sediment. Res. 76, 1304–1322. doi: 10.2110/jsr.2006.106

Goldstein, T.J., Reynolds, R.H., 1994. Systematics of fluid inclusions in diagenetic minerals. SEPM Short Course 31, pp. 199.

Grandia, F., Cardellach, E., Canals, A., 2001. Estudio petrográfico de las mineralizaciones de Zn-Pb de Riópar (Provincia de Albacete, España). Unpublished report.

Grandia, F., Cardellach, E., Canals, A., Banks, C.J., 2003. Geochemistry of the fluids related to epigenetic carbonate-hosted Zn-Pb deposits in the Maestrat Basin, Eastern Spain: fluid inclusion and isotope (Cl, C, O, S, Sr) evidence. Econ. Geol. 98(5), 933-954. doi: 10.2113/gsecongeo.98.5.933

Gregg, J.M., Sibley, D.F., 1984. Epigenetic dolomitization and the origin of xenotopic dolomite texture. J. Sediment. Petrol. 54, 908–931. doi: 10.1306/212F8A30-2B24-11D7-8648000102C1865D

Hanne, D., White, N., Lonergan, L., 2003. Subsidence analyses from the Betic Cordillera, southeast Spain. Basin Res. 15, 1–21. doi: 10.1046/j.1365-2117.2003.00192.x

Hannigan, P.K., Dixon, L., Morrow, D.W., 2006. Oil and gas potential of the Northern Mainland, Canada (Mackenzie Corridor and Northern Yukon). Geol. Surv. Can., Open File 5343 (CDRom).

Hudson, J.D., 1977. Stable isotopes and limestone lithification. J. Geol. Soc. Lond. 133, 637-660. doi: 10.1144/gsjgs.133.6.0637

Kesler, S.E., 1996. Appalachian Mississippi Valley-type deposits: Paleoaquifers and brine provinces, in: Sangster, D.F. (Ed.), Carbonate hosted lead-zinc deposits. Society of Economic Geologists Special Publication 4, pp. 29-57.

Land, L.S., 1985. The origin of massive dolomite. J. Geol. Educ. 33, 112–125.

Land, L.S., 1983. The application of stable isotope studies of the origin of dolomite and to problems of diagenesis of clastic sediments, in: Arthur, M.A., Anderson, T.F. (Eds.), Stable Isotopes in Sedimentary Geology. Society of Economic Paleontologists and Mineralogists Short Course, pp. 1–22.

Lapponi, F., Casini, G., Sharp, I., Blendinger, W., Fernandez, N., Romaire, I., Hunt, D., 2011. From outcrop to 3D modelling: a case study of a dolomitized carbonate reservoir, Zagros Mountains, Iran, in: Hollis, C., Sharp, I. (Eds.), Albian-Cenomanian-Turonian Carbonate-Siliciclastic Systems of the Arabian Plate; Advances in Diagnosis, Structure and Reservoir Modeling. Petroleum Geoscience, pp. 283–307. doi: 10.1144/1354-079310-040

Leach, L.F., Sangster, D.F., 1993. Mississippi Valley-type lead-zinc deposits, in: Kirkham, R.V., Sinclair, W.D., Thorpe, R.I., Duke, J.M. (Eds.), Mineral Deposits Modeling. Geological Association of Canada Special Paper, pp. 289–314.

López-Horgue, M.A., Iriarte, E., Schröder, S., Fernández-Mendiola, P.A., Caline, B., Corneyllie, H., Frémont, J., Sudrie, M., Zerti, S., 2010. Structurally controlled hydrothermal dolomites in Albian carbonates of the Asón valley, Basque Cantabrian Basin, Northern Spain. Mar. Pet. Geol. 27, 1069–1092. doi: 10.1016/j.marpetgeo.2009.10.015

Martín-Chivelet, J., 1994. Litoestratigrafía del Cretácico superior del Altiplano de Jumilla-Yecla (Zona Prebética). Cuad. Geol. Ibérica 18, 117–173.

Martín-Martín, J.D., Gomez-Rivas, E., Bover-Arnal, T., Travé, A., Salas, R., Moreno-Bedmar, J.A., Tomás, S., Corbella, M., Teixell, A., Vergés, J., Stafford, S.L., 2013. The Upper Aptian to Lower Albian syn-rift carbonate succession of the southern Maestrat Basin (Spain): Facies architecture and fault-controlled stratabound dolostones. Cretac. Res. 41, 217–236. doi: 10.1016/j.cretres.2012.12.008

Merino, E., Canals, À., 2011. Self-accelerating dolomite-for-calcite replacement: Self-organized dynamics of burial dolomitization and associated mineralization. Am. J. Sci. 311, 573–607. doi: 10.2475/07.2011.01

Montenat, C., Ott d'Estavou, P., Pierson D'Autrey, P., 1996. Miocene basins of the eastern Prebetic zone: some tectonosedimentary aspects, in: Friend, P.F., Dabrio, C.J. (Eds.), Tertiary Basins of Spain: The Stratigraphic Record of Crustal Kinematics. Cambridge University Press, Cambridge, World and regional geology 6, pp. 346–352.

Morrow, D.W., 1990. Dolomite - Part 1: the chemistry of dolomitization and dolomite precipitation, in: McIlreath, I.A., Morrow, D.W. (Eds.), Diagenesis. Geoscience Canada Reprint Series 4, Ottawa, pp. 113–124.

Morrow, D.W., 2014. Zebra and boxwork fabrics in hydrothermal dolomites of northern Canada: Indicators for dilatational fracturing, dissolution or *in situ* replacement? Sedimentology, 61, 915–951. doi: 10.1111/sed.12094

Muchez, P., Heijlen, W., Banks, D., Blundell, D., Boni, M., Grandia, F., 2005. Extensional tectonics and the timing and formation of basin-hosted deposits in Europe. Ore Geol. Rev. 27, 241–267. doi: 10.1016/j.oregeorev.2005.07.013

Pérez-Valera, L.A., Sánchez-Gómez, M., Fernández-Soler, J.M., Pérez-Valera, F., Azor, A., 2010. Diques de lamproítas a lo largo de la falla de Socovos (Béticas orientales. Geogaceta 48, 151-154.

Rodríguez-Estrella, T., 1979. Geología e Hidrogeología del Sector de Alcaraz - Liétor - Yeste (Provincia de Albacete). Instituto Geológico i Minero de España 97, pp. 566.

Rodríguez-Pascua, M.A., Calvo, J.P., De Vicente, G., Gómez-Gras, D., 2000. Soft-sediment deformation structures interpreted as seismites in lacustrine sediments of the Prebetic Zone, SE Spain, and their potential use as indicators of earthquake magnitudes during the Late Miocene. Sediment. Geol. 135, 117–135. doi: 10.1016/S0037-0738(00)00067-1

Sharp, I., Gillespie, P., Morsalnezhad, D., Taberner, C., Karpuz, R., Vergés, J., Horbury, A., Pickard, N., Garland, J., Hunt, D., 2010. Stratigraphic architecture and fracture-controlled dolomitization of the Cretaceous Khami and Bangestan groups: an outcrop case study, Zagros Mountains, Iran. Geol. Soc. London, Spec. Publ. 329, 343–396. doi: 10.1144/SP329.14

Shelton, K.L., Bauer, R.M., Gregg, J.M., 1992. Fluid-inclusion studies of regionally extensive epigenetic dolomites, Bonneterre Dolomite (Cambrian), southeast Missouri: evidence of multiple fluids during dolomitization and lead-zinc mineralization. Geol. Soc. Am. Bull. 104, 675–683. doi: 10.1120/0016-7606(1992)104<0675:FISORE>2.3.CO;2

Sibley, D.F., Gregg, J.M., 1987. Classification of dolomite rock textures. J. Sediment. Res. 57, 967–975. doi: 10.1306/212F8CBA-2B24-11D7-8648000102C1865D

Smith, L.B., Davies, G.R., 2006. Structurally controlled hydrothermal alteration of carbonate reservoirs: Introduction. Am. Assoc. Pet. Geol. Bull. 90, 1635–1640. doi: 10.1306/intro901106

Swart P.K, Cantrell D.L, Westphal H., Handford R., Kendall C.G., 2005. Origin of dolomite in the arab-D reservoir from the Ghawar field, Saudi Arabia. Evidence from petrographic and geochemical constraints. J. Sedimt. Res. 75, 476–491. doi: 10.2110/jsr.2005.037

Veizer, J., Ala, D., Azmy, K., Bruckschen, P., Buhl, D., Bruhn, F., Carden, G.A.F., Diener, A., Ebneth, S., Godderis, Y., Jasper, T., Korte, C., Pawellek, F., Podlaha, O.G., Strauss, H., 1999. $^{87}Sr/^{86}Sr$, $\delta^{13}C$ and $\delta^{18}O$ evolution of Phanerozoic seawater. Chem. Geol. 161, 59–88. doi: 10.1016/S0009-2541(99)00081-9

Vera, J.A., Arias, C., García-Hernández, M., López-Garrido, A.C., Martín-Algarra, A., Martín-Chivelet, J., Molina, J.M., Rivas, P., Ruiz-Ortiz, P.A., Sanz de Galdeano, C., Vilas, L., 2004. Las zonas externas béticas y el paelomargen sudibérico, in: Vera, J.A. (Ed.), Geología de España. Sociedad Geológica de España e Instituto Geológico de España, pp. 354–360.

Vilas, L., Dabrio, C., Peláez, J.R., García-Hernández, M., 2001. Dominios sedimentarios generados durante el periodo extensional Cretácico Inferior entre Cazorla y Hellín (Béticas Externas). Su implicación en la estructural actual. Rev. Soc. Geol. España 14, 113–122.

Warren, J., 2000. Dolomite: occurrence, evolution and economically important associations. Earth-Science Rev. 52, 1–81. doi:10.1016/S0012-8252(00)00022-2

White, D.E., 1957. Thermal waters of volcanic origin. Geol. Soc. Am. Bull. 68, 1637–1658. doi: 10.1130/0016-7606(1957)68[1637:TWOVO]2.0.CO;2

Wilson, M.E.J., Evans, M.J., Oxtoby, N.H., Nas, D.S., Donnelly, T., Thirlwall, M., 2007. Reservoir quality, textural evolution, and origin of fault-associated dolomites. Am. Assoc. Pet. Geol. Bull. 91 (9), 1247–1272. doi: 10.1306/05070706052

Zenger, D.H., Dunham, J.B., Ethington, R.L., 1980. Concepts and models of dolomitization. Soc. Econ. Paleontol. Mineral. Spec. Publ. 28, 426.

Zheng, Y.F., Hoefs, J., 1993. Carbon and oxygen isotopic covariations in hydrothermal calcites: Theoretical modeling on mixing processes and application to Pb-Zn deposits in the Harz Mountains, Germany. Miner. Depos. 28, 79–89. doi: 10.1007/BF00196332